The Astrophysical Journal, 948:130 (20pp), 2023 May 10 https://doi.org/10.3847/1538-4357/acbef9

Electron Reacceleration via Ion Cyclotron Waves in the Intracluster Medium

Aaron Tran[1], Lorenzo Sironi[1], Francisco Ley[2], Ellen G. Zweibel[2,3], and Mario A. Riquelme[4]
[1] Department of Astronomy, Columbia University, 550 W 120th St., MC 5246, New York, NY 10027, USA; aaron.tran@columbia.edu, lsironi@astro.columbia.edu
[2] Department of Astronomy, University of Wisconsin-Madison, 475 N Charter St., Madison, WI 53706, USA
[3] Department of Physics, University of Wisconsin-Madison, 1150 University Ave., Madison, WI 53706, USA
[4] Departamento de Física, Facultad de Ciencias Físicas y Matemáticas, Universidad de Chile, Av. Blanco Encalada 2008, Santiago, Chile
Received 2022 September 24; revised 2023 February 8; accepted 2023 February 20; published 2023 May 16

Abstract

In galaxy clusters, the intracluster medium (ICM) is expected to host a diffuse, long-lived, and invisible population of "fossil" cosmic-ray electrons (CRe) with 1–100 MeV energies. These CRe, if reaccelerated by 100× in energy, can contribute synchrotron luminosity to cluster radio halos, relics, and phoenices. Reacceleration may be aided by CRe scattering upon the ion-Larmor-scale waves that spawn when ICM is compressed, dilated, or sheared. We study CRe scattering and energy gain due to ion cyclotron (IC) waves generated by continuously driven compression in 1D fully kinetic particle-in-cell simulations. We find that pitch-angle scattering of CRe by IC waves induces energy gain via magnetic pumping. In an optimal range of IC-resonant momenta, CRe may gain up to ∼10%–30% of their initial energy in one compression/dilation cycle with magnetic field amplification ∼3–6×, assuming adiabatic decompression without further scattering and averaging over initial pitch angle.

Unified Astronomy Thesaurus concepts: Intracluster medium (858); Plasma astrophysics (1261); Cosmic rays (329); Non-thermal radiation sources (1119)

Supporting material: machine-readable table

1. Introduction

Clusters of galaxies host hot, diffuse, X-ray emitting gas, which we call the intracluster medium (ICM). Some clusters, especially disturbed and merging clusters, also host a rich variety of diffuse MHz–GHz radio emission in their ICM: radio synchrotron halos, bridges, relics, and phoenices powered by relativistic cosmic-ray electrons (CRe; van Weeren et al. 2019). These CRe cool via synchrotron radiation and inverse-Compton scattering off cosmic microwave background photons over megayears to gigayears, reaching 1–100 MeV energies. Because radiative power losses decrease at lower electron energies, and Coulomb collisions are weak in the ICM, MeV "fossil" CRe may persist in clusters for $\gtrsim$Gyr (Enßlin 1999; Petrosian 2001; Pinzke et al. 2013).

Fossil CRe energies are too low to emit detectable radio synchrotron emission. However, a reacceleration of 100× in energy can make fossil CRe shine again in radio synchrotron and permit them to contribute to the power budget of radio emission in the ICM (Brunetti et al. 2001; van Weeren et al. 2019; Brunetti & Vazza 2020). Many mechanisms can energize fossil CRe: large-scale adiabatic compression from subsonic sloshing or shocks (Enßlin & Gopal-Krishna 2001; Markevitch et al. 2005), diffusive shock acceleration in cluster merger shocks (Kang et al. 2012; Guo et al. 2014; Kang & Ryu 2016; van Weeren et al. 2017; Ha et al. 2022), and wave damping or reconnection within a turbulent scale-by-scale cascade (Brunetti & Lazarian 2007, 2011, 2016).

We consider another possibility for reaccelerating fossil CRe, wherein large-scale deformation—compression, dilation, or shear—drives small-scale plasma waves that might directly scatter and energize CRe. When the ICM deforms on timescales shorter than the Coulomb collision time and longer than the Larmor gyration time, the $\boldsymbol{B}$-perpendicular temperature $T_\perp$ changes due to conservation of particle magnetic moment ${p_\perp}^2/B$, and the $\boldsymbol{B}$-parallel temperature $T_\parallel$ changes due to conservation of particle bounce invariant $\oint p_\parallel\, ds$ integrated along a field line (assuming periodicity in parallel motion). As $T_\perp$ and $T_\parallel$ evolve independently, the plasma becomes temperature and pressure anisotropic: $\Delta \equiv T_\perp/T_\parallel - 1 \neq 0$. Because the ICM's thermal pressure dominates over magnetic pressure, i.e., its plasma beta $\beta_\mathrm{p} = P_\mathrm{thermal}/P_\mathrm{magnetic} \gg 1$, $\Delta \neq 0$ easily triggers the growth of various Larmor-scale plasma waves (Kasper et al. 2002; Bale et al. 2009; Kunz et al. 2014, 2019). The strongest waves reside at proton Larmor scales; although they are triggered by and regulated by proton anisotropy, they may also interact with fossil CRe, which gyrate more slowly and have larger Larmor radii than typical ICM thermal electrons.

We focus on CRe interaction with ion cyclotron (IC) waves driven by thermal ICM proton (i.e., ion) anisotropy $\Delta > 0$, with the anisotropy in turn driven by continuous compression. IC waves interact with electrons via the gyroresonance condition:

$$\omega - k v_\parallel = -|\Omega_\mathrm{e}|/\gamma, \tag{1}$$

where ω is wave angular frequency, $k = 2\pi/\lambda$ is wavenumber, λ is wavelength, $v_\parallel$ is electron velocity parallel to $\boldsymbol{B}$, $\Omega_\mathrm{e} = -eB/(m_\mathrm{e}\, c)$ is the signed nonrelativistic electron cyclotron frequency, and γ is the electron's Lorentz factor. Equation (1) specifies an "anomalous" resonance, wherein an electron overtaking the wave ($|v_\parallel| > |\omega/k|$) sees the Doppler-shifted IC wave polarization as right-circular rather than left-circular, thus enabling gyroresonance (Tsurutani & Lakhina 1997; Terasawa & Matsukiyo 2012). The resonance condition is simplified in the low-frequency limit, appropriate for ICM plasma with Alfvén speed $v_\mathrm{A}/c \ll 1$ and ion–electron mass

ratio $m_i/m_e \gg 1$:

$$\frac{p_\parallel}{m_e c} \approx \frac{|\Omega_e|}{kc} \approx \frac{1}{k\rho_i}\left(\frac{v_{th,i}}{c}\right)\left(\frac{m_i}{m_e}\right). \quad (2)$$

Here, $v_{th,i} = \sqrt{3k_B T_i/m_i}$ is the ion thermal velocity. The form of Equation (2) anticipates that k^{-1} is on the order of the ion Larmor radius ρ_i for temperature-anisotropy-driven IC waves at marginal stability (Davidson & Ogden 1975; Yoon et al. 2010; Sironi & Narayan 2015).[5] For ICM temperatures $T_i \approx T_e \sim 1$–10 keV (Chen et al. 2007), IC waves with $k\rho_i \sim 0.5$, and $m_i/m_e = 1836$ for a proton–electron plasma, we anticipate resonant momenta $p_\parallel \sim 7$ to $21\, m_e c$ within the expected range for fossil CRe in the ICM, $p \sim 1$ to $300\, m_e c$ (Pinzke et al. 2013). We thus expect that IC waves may efficiently scatter fossil CRe.

Gyroresonant IC wave scattering may energize CRe in at least two different ways. First, the nonzero phase velocity of IC waves will transfer energy from waves to CRe via second-order Fermi acceleration (Fermi 1949), but this is slow because the energy gain per cycle scales with the square of the scatterers' velocity, $(v_A/c)^2 \ll 1$ for IC waves. Second, pitch-angle scattering couples parallel and perpendicular momenta $p_\parallel$, $p_\perp$ and drives CRe toward isotropy. Pitch-angle scattering, in isolation, conserves particle energy. However, scattering during bulk deformation can heat particles via magnetic pumping if the scattering rate is comparable to the bulk deformation rate (Berger et al. 1958; Lichko et al. 2017).

Magnetic pumping in a compressing plasma works as follows. Because particle momenta $p_\perp$ and $p_\parallel$ have different adiabatic responses to compression, a scattering rate comparable to the bulk compression rate can cause a net transfer of energy from $p_\perp$ to $p_\parallel$ over one compression–decompression cycle; this energy transfer may be linked to a phase difference between pressure anisotropy and magnetic field compression (Lichko et al. 2017). Magnetic pumping has been previously studied in the contexts of plasma confinement, planetary magnetospheres, and the solar wind (Alfvén 1950; Schlüter 1957; Berger et al. 1958; Goertz 1978; Borovsky et al. 1981, 2017; Borovsky 1986; Lichko et al. 2017; Fowler et al. 2020; Lichko & Egedal 2020).

In high-β_p plasmas with $\Delta > 0$, anisotropy-driven IC waves may not be the dominant fluctuations. Nonpropagating structures created by the mirror instability are thought to prevail over IC waves, based on theory (e.g., Shoji et al. 2009; Isenberg et al. 2013) and measurements in Earth's magnetosheath (Schwartz et al. 1996) and the solar wind (Bale et al. 2009). Nevertheless: IC waves may coexist with mirror structures; IC waves appear in 3D hybrid simulations of turbulent high-β_p plasma (Markovskii et al. 2020; Arzamasskiy et al. 2023); there may be local regions of the ICM with reduced plasma β_p or with reduced electron/ion temperature ratio T_e/T_i (Fox & Loeb 1997) more conducive for IC wave growth. Mirror modes also have $k \sim \rho_i^{-1}$, so they may nonresonantly scatter fossil CRe and drive magnetic pumping as well. The same will likely hold for firehose modes excited when $\Delta < 0$.

[5] For $kc/\omega_{pi} = \Delta/\sqrt{\Delta+1}$ at marginal stability (Equation (6) in Davidson & Ogden 1975), adopting $\Delta = S/\beta_{i\parallel}^{0.5}$ with order-unity constant S (Sironi & Narayan 2015) yields $k\rho_i \approx S$ for $\Delta \ll 1$. Here c/ω_{pi} is the ion skin depth, and $\beta_{i\parallel}$ is the $\boldsymbol{B}$-parallel ion beta.

IC-resonant scattering of relativistic MeV electrons also occurs in Earth's radiation belts and can precipitate electrons into the upper atmosphere (e.g., Thorne & Kennel 1971; Meredith et al. 2003; Zhang et al. 2016; Adair et al. 2022). In particular, Borovsky et al. (2017) studied the same mechanism as this article—compression-driven IC waves energizing relativistic electrons via magnetic pumping—applied to Earth's outer radiation belt.

2. Methods

We simulate continuously compressed ICM plasma using the relativistic particle-in-cell (PIC) code TRISTAN-MP (Buneman 1993; Spitkovsky 2005). The PIC equations are solved in comoving coordinates while subject to global compression or expansion, as implemented by Sironi & Narayan (2015), similar to hybrid expanding box simulations in the literature (Liewer et al. 2001; Hellinger et al. 2003; Hellinger & Trávníček 2005; Innocenti et al. 2019; Bott et al. 2021). To do this, Sironi & Narayan (2015) transform from the physical laboratory frame (t_{lab}, $\boldsymbol{x}_{lab}$) to a comoving coordinate frame (t', $\boldsymbol{x}'$) via a transformation law $\boldsymbol{x}_{lab} = \boldsymbol{L}\boldsymbol{x}'$, where:

$$\boldsymbol{L} = \begin{pmatrix} a_x(t) & 0 & 0 \\ 0 & a_y(t) & 0 \\ 0 & 0 & a_z(t) \end{pmatrix},$$

and the differential transformation law is:

$$d\boldsymbol{x}_{lab} = \boldsymbol{L}d\boldsymbol{x}' + \dot{\boldsymbol{L}}\boldsymbol{x}'dt'.$$

The scale factors a_x, a_y, and a_z are >1 for expansion and <1 for contraction. We report quantities (fields, particle positions, momenta, distribution function moments) in physical CGS units in the plasma's local rest frame; i.e., the unprimed coordinates $d\boldsymbol{x} = \boldsymbol{L}d\boldsymbol{x}'$ of Sironi & Narayan (2015).

We use a 1D domain parallel to a background magnetic field $\boldsymbol{B}$, which permits the growth of parallel-propagating IC waves and precludes the growth of the mirror instability. Our domain and magnetic field $\boldsymbol{B}$ are aligned along y; all wavenumbers $k \equiv k_y$ in this article. We compress along both x and z axes by choosing scale factors:

$$a_x(t) = a_z(t) = \frac{1}{1+qt}, \quad (3)$$

where $q > 0$ is a tunable constant controlling the compression rate. We fix $a_y(t) = 1$. The background field evolves consistent with flux freezing as

$$B_y = B_g(t) = B_0(1+qt)^2,$$

where B_0 is the initial field strength. The imposed $\boldsymbol{B}$-perpendicular compression conserves two particle invariants, ${p_\perp}^2/B$ and $p_\parallel$, if there is no wave–particle interaction (Sironi & Narayan 2015, Appendix A.2).

The ICM is modeled as a thermal ion–electron plasma with Maxwell–Jüttner distributions of initial temperature T_0 and density n_0 for each species. The fossil CRe are modeled as test particles, i.e., passive tracer particles, which advance according to the electromagnetic fields on the grid but do not contribute to

the plasma dynamics—in the PIC algorithm, they have no weight and so deposit no current. The treatment of fossil CRe as passive tracers is motivated by their low kinetic energy density, $\sim 10^4\times$ smaller than the thermal ICM, in cluster outskirts as simulated by Pinzke et al. (2013, Figure 3). However, fossil CRe could become dynamically important in the recently shocked ICM responsible for radio relics; see, e.g., Böss et al. (2023, Figure 11) and Ha et al. (2022).

Standard length- and timescales are defined as follows for thermal plasma species $s \in \{\mathrm{i}, \mathrm{e}\}$. The signed, nonrelativistic particle cyclotron frequency $\Omega_\mathrm{s} = q_\mathrm{s}\ B/(m_\mathrm{s}\ c)$. The plasma frequency $\omega_\mathrm{ps} = \sqrt{4\pi n_\mathrm{s} e^2/m_\mathrm{s}}$. The Larmor radius $\rho_\mathrm{s} = m_\mathrm{s}\ v_\mathrm{th,s}\ c/(eB)$, where $v_\mathrm{th,s} = \sqrt{3k_\mathrm{B}T_\mathrm{s}/m_\mathrm{s}}$ is a thermal velocity. Subscript 0 in Ω_s0, ω_ps0, ρ_s0, and other symbols hereafter means that the quantity is evaluated at $t = 0$. Subscripts $\perp$ and $\parallel$ indicate vector projections with respect to the background magnetic field direction $\hat{y}$.

Our results center on one "fiducial" simulation with ion-to-electron mass ratio $m_\mathrm{i}/m_\mathrm{e} = 8$, initial plasma beta $\beta_\mathrm{p0} = 16\pi n_0 k_\mathrm{B} T_0/{B_0}^2 = 20$, initial Alfvén speed $v_\mathrm{A0}/c = B_0/\sqrt{4\pi(m_\mathrm{i} + m_\mathrm{e})n_0 c^2} = 0.067$, and compression timescale $q^{-1} = 800\Omega_\mathrm{i0}^{-1}$. The choice of v_A0/c is equivalent to choosing an initial temperature of $k_\mathrm{B}\ T_0/(m_\mathrm{e}\ c^2) = 0.2$ for fixed β_p0. We use 16,384 particles per cell for the thermal plasma (i.e., 8192 ions and 8192 electrons per cell); Appendix E shows convergence with respect to the number of particles per cell. The plasma skin depth $c/\sqrt{\omega_\mathrm{pe0}^2 + \omega_\mathrm{pi0}^2}$ is resolved with five cells. The domain size is $4608\,\mathrm{cells} = 307.2\mathrm{c}/\omega_\mathrm{pi0} = 79.3\rho_\mathrm{i0}$. The Debye length $\lambda_\mathrm{De} = \sqrt{k_\mathrm{B}T_0/(4\pi n_0 e^2)}$ is resolved with 2.4 cells. The numerical speed of light is 0.25 grid cells per simulation time step to ensure that the Courant–Friedrichs–Lewy condition is satisfied for smaller physical cell lengths at late simulation times (Sironi & Narayan 2015, Appendix A.1). In each time step, the electric current is smoothed with 32 passes of a three-point binomial ("1-2-1") filter, approximating a Gaussian filter with a standard deviation of four cells (Birdsall & Langdon 1991, Appendix C). Outputs are saved at $\sim 1\Omega_\mathrm{i0}^{-1}$ intervals.

We use two different initial test-particle CRe distributions $f(p)\mathrm{d}p$ depending on our analysis needs: $f(p)$ constant (flat) or $f(p) \propto p^{-1}$ to uniformly sample p or $\log p$, respectively. Both distributions are isotropic. The $f(p)$ constant case uses 2,880,000 CRe in $p = 0$ to $70\,m_\mathrm{e}\ c$, and the $f(p) \propto p^{-1}$ case uses 14,400,000 CRe in $p = 0.0014$ to $1400\,m_\mathrm{e}\ c$. Neither case mimics nature, but the uniform p and $\log p$ sampling means that our results can be reweighted to describe any initially isotropic CRe distribution. The test-particle distributions span the momentum range of CRe that should be efficiently scattered by IC waves in our simulation: $p_\parallel \sim 4$ to $25\,m_\mathrm{e}\ c$ based on Equation (2).[6]

Besides our fiducial simulation, we also run simulations with varying q, $m_\mathrm{i}/m_\mathrm{e}$, v_A0/c, and β_p0; the detailed parameters are given in Appendix F and Table 1. The domain size is pinned to $\sim 80\rho_\mathrm{i0}$ for all such simulations. The test-particle CRe spectrum is kept flat ($f(p)$ constant), but the upper bound is rescaled according to $(m_\mathrm{i}/m_\mathrm{e})(v_\mathrm{th,i}/c)$ per Equation (2) to capture the momentum range of the expected IC gyroresonance. The simulations with varying β_p0 are not presented in the main text and appear only in Appendix B. In cases with slow compression, e.g., $q^{-1}/\Omega_\mathrm{i0}^{-1} = 3200$ or $m_\mathrm{i}/m_\mathrm{e} = 32$ in Table 1, we saw gyrophase-dependent numerical errors in particle momenta when using single-precision (32 bit) floats in the PIC algorithm. We therefore use double-precision (64 bit) floats for all simulations in the article, except for convergence checks in Appendix E.

Besides IC waves, whistlers (i.e., electron cyclotron waves) are excited by the thermal electrons in our simulations. To help separate the effects of whistler and IC waves upon fossil CRe energy gain, we perform simulations in which one particle species, ions or electrons, is compressed isotropically in order to suppress that species' cyclotron waves. The species may still participate in plasma dynamics by generating currents. To implement isotropic compression, we modify the comoving momentum equation (Boris particle push):

$$\frac{d\boldsymbol{p}}{dt} = -\dot{\boldsymbol{L}}\boldsymbol{L}^{-1}\boldsymbol{p} + q\left(\boldsymbol{E} + \frac{\boldsymbol{v}}{c} \times \boldsymbol{B}\right). \tag{4}$$

For the chosen species, we set the diagonal elements of $\dot{\boldsymbol{L}}\boldsymbol{L}^{-1}$ in the Boris pusher to $a_x = a_y = a_z = 1/(1 + q_\mathrm{iso}\ t)$. We choose $q_\mathrm{iso} = 2q/3$ to match the initial energy input rate from anisotropic compression; i.e., at $t = 0$, the determinant $\ell \equiv \det \boldsymbol{L} = 1/(1 + q_\mathrm{iso}t)^3$ has first derivative equal to that for the anisotropic $\ell = 1/(1 + qt)^2$. The rest of the code in the PIC algorithm retains the anisotropic compression. For electrons, isotropic forcing is only applied to regular particles (thermal ICM) and not test particles (fossil CRe).

3. Wave Properties

3.1. Time Evolution

The simulation evolves as follows. The compression at first drives $T_\perp \propto B_g(t) > T_\parallel =$ constant for all species while conserving the adiabatic invariants of magnetized particles (Northrop 1963), which can be recast according to the Chew–Goldberger–Low (CGL) fluid theory as pressure or temperature invariants (Chew et al. 1956). Instability is triggered, and waves grow, between $t = 0.2q^{-1}$ and $0.5q^{-1}$ (Figures 1(a)–(c)). Right-circularly polarized (RCP) whistlers appear first and are the dominant mode at $t = 0.2q^{-1}$, followed by left-circularly polarized (LCP) ion cyclotron waves from $t = 0.3$ to $0.5q^{-1}$. The wave polarizations are distinguished by Fourier transform of $B_z + iB_x$ in Figure 1(a), which separates LCP and RCP waves into $\omega > 0$ and <0, respectively, following Ley et al. (2019). The wave fluctuation power $(\delta B_\perp/B_g)^2$ saturates at a near-constant or slightly decreasing level by $t \sim 0.55q^{-1}$ (Figure 1(c)); while saturated, the IC wave power drifts toward lower ω and k (Figures 1(a)–(b)). We plot a manually chosen approximation to the k-space drift,

$$k_\mathrm{IC}(t) = [0.09 + 0.18(1.5 - qt)^5]\omega_\mathrm{pi0}/c, \tag{5}$$

in Figure 1(b), to be used later in this article (Section 7).

The saturated waves drive the ion and electron temperature anisotropy Δ away from CGL-invariant conservation and toward a marginally stable state at late times $t \gtrsim 1q^{-1}$ (Figure 1(d)). At marginal stability, we expect $\Delta \propto \beta_\mathrm{s\parallel}^{-0.5}$ for both ions (Gary & Lee 1994; Gary et al. 1994b; Hellinger et al. 2006) and electrons (Gary & Wang 1996; Gary & Karimabadi 2006), where $\beta_\mathrm{s\parallel} = 8\pi n(t) k_\mathrm{B} T_\mathrm{s\parallel}(t)/B_g(t)^2$. We fit the

[6] Assuming $k\ \rho_\mathrm{i} \sim 0.5$ and $B_g(t)$ increasing $6\times$ from $t = 0$ to $1.5q^{-1}$.

relation $\Delta \propto A_s \beta_{s\parallel}^{-0.5}$ between $t = 1q^{-1}$ and the simulation's end to obtain $A_i = 0.98 \pm 0.02$ and $A_e = 0.785 \pm 0.012$; the best-fit relations are the dotted lines in Figure 1(d). The uncertainty on A_i and A_e is one standard deviation estimated by assuming $\chi^2_{\text{reduced}} = 1$, as no data uncertainty is used in fitting. We expect that the systematic uncertainty is larger.

When the IC waves saturate, we expect balance between compression increasing Δ and wave pitch-angle scattering decreasing Δ, as suggested by the marginal-stability scaling in Figure 1(d). This balance may be stated as:

$$\frac{d\Delta}{dt} = \frac{\dot{B}}{B}(\Delta + 1) - \nu\Delta(2\Delta + 3) \approx 0, \tag{6}$$

which we obtain from moments of the Vlasov equation with a Lorentz-operator scattering frequency ν constant with respect to momentum p and pitch-angle cosine $\mu \equiv p_\parallel/p$ (Appendix A), using a drift-kinetic model as in Zweibel (2020) and Ley et al. (2023) and following a similar argument as in Kunz et al. (2020, Section 3.1.2). If scattering scales like the quasi-linear approximation, $\nu \propto \delta B_\perp{}^2$, then we expect

$$\left(\frac{\delta B_\perp}{B_g(t)}\right)^2 \propto \frac{\nu}{\Omega_i(t)} \approx \left(\frac{\dot{B}/B}{\Omega_i(t)}\right)\frac{\Delta_i + 1}{\Delta_i(2\Delta_i + 3)}. \tag{7}$$

In taking $\Delta = \Delta_i$, we assume that only ions source and control the wave power $(\delta B_\perp/B)^2$ at late times. In Figure 1(c), we show Equation (7) computed with arbitrary normalization and using $\Delta_i = T_{i\perp}/T_{i\parallel} - 1$ measured from the simulation. Equation (7) does not explain the total late-time wave power in our simulation, but it better matches the power in currently unstable IC waves (Figures 1(a), (c)). We conjecture that waves in the unstable IC region may be most important for regulating Δ_i, in contrast to the stronger IC wave power at lower k.

The total plasma beta decreases to half its initial value by the simulation's end, with ions hotter than electrons (Figure 1(e)). At early times $t \lesssim 0.1q^{-1}$, $\beta_{e\perp}$ deviates from the nonrelativistic CGL prediction because electrons are almost relativistic with $k_B\, T_0 = 0.2\, m_e\, c^2$.

3.2. Wave Identification

Let us now more closely study the wave properties and evolution. To predict the wave ω, k, and damping/growth as a function of time, we solve the nonrelativistic dispersion relation for $\boldsymbol{B}$ -parallel electromagnetic waves in a bi-Maxwellian ion–electron plasma:

$$D^\pm = 1 - \frac{k^2c^2}{\omega^2} + \sum_s \left(\frac{\omega_{ps}}{\omega}\right)^2 \left[\zeta_0 Z(\zeta_{\pm 1}) - \frac{1}{2}\left(\frac{T_{s\perp}}{T_{s\parallel}} - 1\right) Z'(\zeta_{\pm 1})\right] \tag{8}$$

as stated in Davidson & Ogden (1975) and Stix (1992, Section 11-2), keeping only the $n = 0, \pm 1$ resonant terms. The subscript $s = i, e$ indexes component species, $Z(\zeta) = 2i \exp(-\zeta^2) \int_{-\infty}^{i\zeta} \exp(-t^2) dt$ is the plasma dispersion function (Fried & Conte 1961), $\zeta_n = (\omega - n\Omega_s)/k_\parallel\, w_{s\parallel}$, and $w_{s\parallel} = \sqrt{2k_B T_{s\parallel}/m_s}$. We approximate $T_{s\parallel}$ and $T_{s\perp}$ using the second moments of the ion and electron distributions in our simulations. In Equation (8), $\omega = \omega_R + i\Gamma$ is complex, but in all other text and figures, ω refers only to the real angular frequency ω_R unless otherwise noted. The imaginary part $\Gamma > 0$ for instability and <0 for damping. We use Equation (8) to show the unstable ω range for LCP waves over time in Figure 1(b), and to show the expected ω and k for both LCP and RCP waves in the ω–k power spectra of Figure 2.

We note several features of interest in the $B_z + iB_x$ spectrogram (Figure 1(b)). LCP and RCP modes both appear at $t \sim 0.2q^{-1}$. The LCP mode is more monochromatic and has lower ω, while the RCP mode has broader bandwidth and higher ω. The LCP modes persist from $t > 0.2q^{-1}$ through the rest of the simulation. The RCP modes appear in two transient bursts, at $t = 0.2$ and $0.4\, q^{-1}$, and the second RCP burst coincides with a growth in the LCP power and near-peak ion anisotropy Δ_i. Some RCP power aliases from $\omega < 0$ into $\omega > 0$ at the top of Figure 1(b) and in each panel of Figure 2.

The LCP power splits into high- and low-frequency bands at $t \approx 0.8$–$1.0q^{-1}$ (Figure 1(a)); each band continues to, respectively, rise and fall in frequency over time. The high-frequency LCP power lies within the expected ω range of IC wave instability as predicted by Equation (8). The low-frequency LCP power resides in a frequency/wavenumber range that is not expected to spontaneously grow IC waves. We remain agnostic about why the low-frequency LCP power evolves toward low k, but we note that Ley et al. (2019, Figure 9) saw a similar drift of the IC wave power to low k in a shearing-box PIC simulation. In Appendix C, we show that wave power drifts to low frequencies even if compression halts at $t = 0.5q^{-1}$, so the low-frequency power drift is not caused by external compression or by a numerical artifact of the comoving PIC domain.

We verify that the LCP and RCP modes are IC waves and whistlers, respectively, by inspecting the ω–k power spectra in three time intervals (Figure 2). The LCP wave power agrees well with the predicted (ω, k) from Equation (8) in all time snapshots of Figure 2, and the previously noted high-frequency band in Figure 1(b) agrees well with the prediction for IC wave instability. The RCP wave power agrees with the bi-Maxwellian whistler dispersion in some respects. The phase speed ω/k agrees with Equation (8) at later times (Figures 2(b)–(c)). In simulations with higher m_i/m_e (Appendix B), the RCP phase speed ω/k increases with respect to the LCP phase speed and continues to agree with Equation (8). However, the RCP wave power disagrees with the bi-Maxwellian dispersion curve in some respects. At early times $t = 0.2$–$0.3q^{-1}$, the RCP mode is offset toward higher k than expected for the whistler mode; it does not appear to lie on a curve passing through $(\omega, k) = (0, 0)$. At later times, the RCP power shows better agreement with the whistler mode: the k offset disappears and RCP power connects continuously to $(\omega, k) = (0, 0)$ (Figures 2(b)–(c)). The later-time RCP power also has ω somewhat lower than that predicted by Equation (8) for $k = 0.5$–$1.0\omega_{pi0}/c$ (Figures 2(b)–(c)). Some more observations on the RCP mode are in Appendix B. All considered, despite the imperfect agreement with Equation (8), we attribute the RCP waves to thermal electron anisotropy and call them whistlers hereafter.

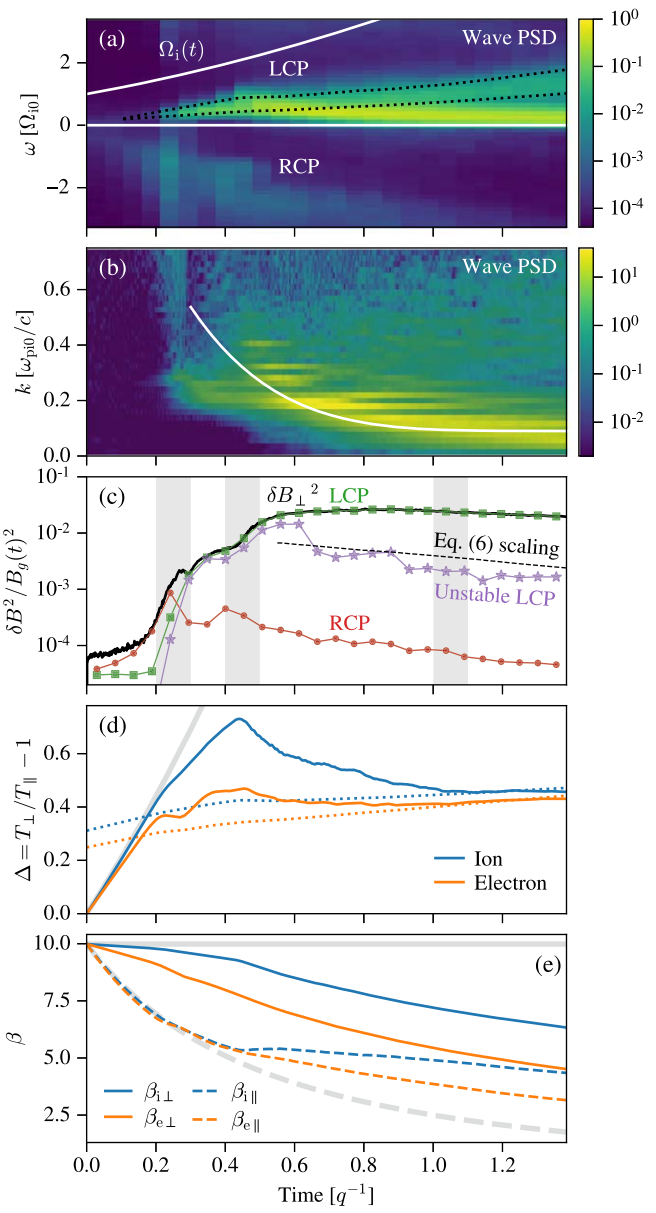

Figure 1. (a) Wave power spectral density (PSD) of $(B_z + iB_x)/B_g(t)$. Left- and right-circularly polarized (LCP, RCP) waves have $\omega > 0$ and $\omega < 0$, respectively. The white line is the ion cyclotron frequency $\Omega_i(t)$. Black dotted lines mark the region of unstable IC waves with linear growth rate $\Gamma > 10^{-3}\,\Omega_{i0}$ from Equation (8). PSD is normalized so that the ω-axis average yields $\delta B_\perp{}^2/B_g(t)^2$. (b) Wave PSD with k on the y-axis. The axis limits omit high-k power to emphasize low-k LCP waves. The white curve is Equation (5) for $t > 0.3q^{-1}$. (c) Total magnetic fluctuation power $\delta B_\perp{}^2/B_g(t)^2$ (solid black). Green squares and red circles, respectively, show the LCP and RCP power from (a). The purple stars show the power within the unstable IC wave region from (a); i.e., PSD between the black dotted lines. The saturated wave scaling Equation (7) (dashed black) is plotted with arbitrary normalization. Gray bands mark the time intervals in Figures 2–3. (d) Ion (blue) and electron (orange) temperature anisotropy with best-fit scalings at marginal stability: $\Delta_i = 0.98\beta_{i\parallel}^{-0.5}$ (dotted blue), $\Delta_e = 0.785\beta_{e\parallel}^{-0.5}$ (dotted orange). (e) Ion and electron plasma beta perpendicular (solid) and parallel (dashed) to $\boldsymbol{B}$; colors as in (d). In (d)–(e), the light-gray curves are nonrelativistic CGL predictions for adiabatic compression.

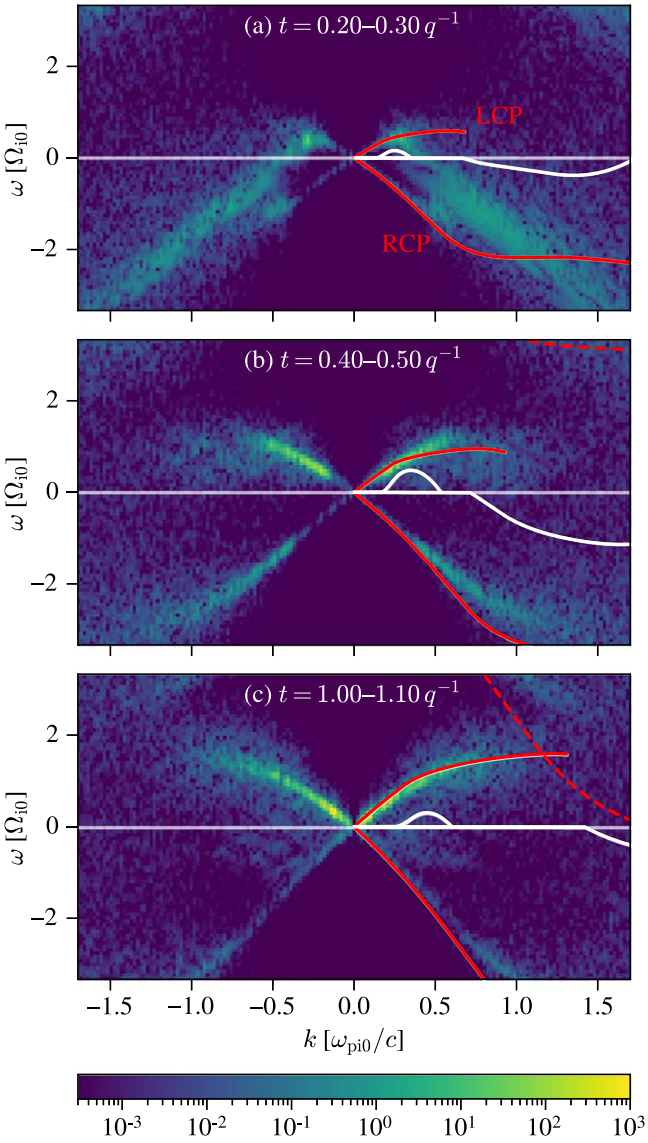

Figure 2. Power spectrum of $B_z + iB_x$ for three different time intervals. Positive/negative ω are LCP/RCP, respectively. The real and imaginary parts of the bi-Maxwellian dispersion relation, $\omega(k)$ and $\Gamma(k)$ computed from Equation (8), are the red and white curves, respectively. Only $\Gamma > 0$, indicating instability, is shown. The IC and whistler growth rates are plotted 5× and 2× larger than their true values for visibility. The dashed red curve is high-frequency whistler mode, aliased due to finite time sampling. The dispersion curves truncate when damping becomes strong, $\Gamma(k) < -|\omega(k)|$.

Equation (8) is approximate, as particles are not exactly bi-Maxwellian. Wave scattering alters distributions to quench instability, and the resulting anisotropic distributions can be stable to ion cyclotron waves (Isenberg et al. 2013). Appendix C checks the frequency of waves driven unstable by the actual particle distribution, and we find that the resulting waves do lie in a high-frequency LCP power band as predicted by Equation (8), validating our use of the bi-Maxwellian approximation in this context.

Equation (8) also does not account for the background plasma density and magnetic field varying during instability growth; the plasma properties are assumed to vary on a much longer timescale than is relevant to the linear dispersion calculation. The maximum IC growth rate predicted by Equation (8) is $\sim 0.1\Omega_{i0}$ at $t \approx 0.5q^{-1}$ (Figure 2(b)), which is 80× faster than the compression rate q. The growth rate may be smaller in practice due to particles quenching their own instability; nevertheless, we expect that waves should grow on a short timescale that is well separated from the compression time.

4. Wave Scattering

Let us compare the CRe scattering directly measured in our simulations against the quasi-linear theory (QLT) description of resonant scattering as a diffusive process, in the limit of weak, uncorrelated, and broadband waves (Jokipii 1966; Kennel & Engelmann 1966; Kennel & Petschek 1966; Kulsrud & Pearce 1969). In particular, we wish to check the following. (1) Do particles with a 90° pitch angle (i.e., $p_\perp \gg p_\parallel$) scatter efficiently in our simulations? As $p_\parallel \to 0$, the resonant wavenumber $k_{\rm res} \to \infty$, and particles cannot scatter at exactly 90° pitch angle in QLT. (2) Does the resonant QLT description hold for our simulations? The saturated wave power $\delta B_\perp/B \sim 0.1$ (Figure 1(a)) may be too strong to satisfy QLT (Liu et al. 2010). Strong waves may lead to, for example, momentum-space advection instead of diffusion (Albert & Bortnik 2009).

We compute the QLT diffusion coefficient $D_{\mu\ \mu}$ for the pitch-angle cosine $\mu = \cos\alpha = p_\parallel/p$, assuming low-frequency ($\omega \approx 0$) waves, following Summers (2005):

$$D_{\mu\mu}(p,\ \mu) \approx (1\ -\ \mu^2)\frac{\pi}{2}\frac{|\Omega_{\rm e}(t)|}{\gamma}\frac{k_{\rm res}W(k_{\rm res})}{B_g(t)^2/(8\pi)}. \quad (9)$$

Because momentum scattering is subdominant in our simulations (Section 9), and is expected to be even more subdominant for lower $v_{\rm A}/c$ in the real ICM, we neglect the QLT diffusion coefficients D_{pp} and $D_{p\ \mu}$ for now. The resonant signed wavenumber is

$$k_{\rm res} = \pm\frac{eB_g(t)}{\mu pc}, \quad (10)$$

with + and − signs for CRe resonance with IC and whistler waves, respectively. We take $W(k)$ to be the two-sided wave power spectrum of $\delta B_\perp^2$ measured directly from our simulation, with the sign of k specifying propagation direction. We decompose $W(k) = W_{\rm L}(k) + W_{\rm R}(k)$ into LCP and RCP pieces by Fourier transforming $B_z + iB_x$ over a time window of length $18.9\Omega_{\rm i0}^{-1}$, which is 4× larger than the time step used to measure particle scattering. The power at $\omega \geqslant 0$ is assigned to $W_{\rm L}$ and the remainder to $W_{\rm R}$. We smooth $W_{\rm R}(k)$ and $W_{\rm L}(k)$ with a Hanning window of length $0.14\omega_{\rm pi0}/c$ (7 points) and then linearly interpolate to compute $D_{\mu\ \mu}$ for arbitrary (p, μ). Because our simulation has balanced forward- and backward-propagating waves, we average $D_{\mu\ \mu}$ over $\mu < 0$ and $\mu > 0$ in Figure 3.

We directly measure $\langle\Delta\mu\Delta\mu\rangle/(2\Delta t)$ by computing $\Delta\mu = \mu(t + \Delta t) - \mu(t)$ over an output time step $\Delta t = 4.7\Omega_{\rm i0}^{-1}$ for each test-particle CRe. The pitch angle α is defined with respect to the background field $B_g(t)\hat{y}$. Then, we compute the particle-averaged $\langle\Delta\mu\Delta\mu\rangle$ as a function of the phase-space coordinates (p, $|\mu|$) using and 140 bins over $p \in [0,\ 70]m_{\rm e}\ c$ and 50 bins over $|\mu| \in [0,\ 1]$. The choice of Δt affects the shape and strength of the scattering regions in Figures 3(j)–(l). We find that time steps $\Delta t = 4.7$–$18.8\ \Omega_{\rm i0}^{-1}$ give somewhat consistent scattering region shapes, but shorter time steps $\Delta t = 0.9$–$1.9\ \Omega_{\rm i0}^{-1}$ do not resolve the scattering interaction, especially for the highest p CRe. Appendix D further shows and discusses the effect of varying Δt in our scattering measurement.

Figure 3 compares the measured pitch-angle scattering rates $\langle\Delta\mu\Delta\mu\rangle/(2\Delta t)$ (Figures 3(j)–(l)) to the predicted rates $D_{\mu\ \mu}$ from LCP (Figures 3(d)–(f)) and RCP (Figures 3(g)–(i)) waves at $t = 0.25$, 0.45, and $1.05q^{-1}$. The smoothed $W_{\rm L}$ and $W_{\rm R}$ used to compute $D_{\mu\ \mu}$ are shown in Figures 3(a)–(c); the one-sided spectra, as normalized, are averages of two-sided spectra over $k > 0$ and $k < 0$. The full QLT prediction for $D_{\mu\ \mu}$ is the sum of the middle two rows (d)–(i), which separate the ion cyclotron and whistler contributions to show their relative importance. White dotted lines mark all particles resonant with a wave of given $k_{\rm res}$ according to Equation (10). At $t = 0.25q^{-1}$ (left column), the whistler power is strong and the particles most efficiently scattered have small momenta $p \sim 1$–$5\ m_{\rm e}\ c$. At $t = 0.45q^{-1}$ (middle column), the ion cyclotron power has overtaken whistlers in strength, with most resonant scattering predicted at the $k = 0.3\omega_{\rm pi0}/c$ contour, though the measured scattering $\langle\Delta\mu\Delta\mu\rangle$ has a broader bandwidth in (p, $|\mu|$) space and does not exactly follow the resonant contour shape of Equation (10). At $t = 1.05q^{-1}$ (right column), the wave power is saturated (Figure 1(a)) and the IC spectrum has broadened to $k = 0.1\ \omega_{\rm pi0}/c$, as seen in both the 1D wave spectrum (top row) and the QLT prediction (second row).

As time progresses, both the measured and modeled scattering extend toward larger p due to two effects. First, the increase in $B_g(t)$ leads to a rightward drift of the resonant contours $p \propto B_g(t)/\mu$ (Equation (10)) for fixed $k_{\rm res}$. Second, the saturated wave power drifts toward smaller k over time (Figures 1(c), 3(b)–(c)). Comparing Figures 3(e) and (f), the QLT-predicted scattering expands from the $k = 0.3\ \omega_{\rm pi0}/c$ contour to $k = 0.1\ \omega_{\rm pi0}/c$ as time progresses. Likewise, comparing Figures 3(k) and (l), the measured scattering expands beyond the $k = 0.1\ \omega_{\rm pi0}/c$ contour. The drift of k-resonant surfaces through momentum space due to both effects allows the cyclotron modes to interact with and scatter a larger volume of CRe than would otherwise be possible.

The measured scattering differs from the QLT prediction in some respects. The scattering region in (p, $|\mu|$) is continuous through the $\mu = 0$ ($\alpha = 90°$) barrier, and the region is more extended in (p, $|\mu|$) space compared to the QLT prediction. Scattering through $\mu = 0$ may be explained by the mirroring of particles with $\mu^2 < (\delta B_\perp/B_g)_{\rm m}^2/2$ (Felice & Kulsrud 2001, Equation (22)), where $(\delta B_\perp/B_g)_{\rm m}^2$ is the power at the specific wavenumber(s) responsible for nonresonant mirroring. The total wave power (Figure 1(a)) sets an upper bound $(\delta B_\perp/B_g)_{\rm m}^2 \lesssim 0.03$, and so we expect mirroring to be important at $|\mu| \lesssim 0.12$. We speculate that resonance broadening (e.g., Tonoian et al. 2022) or a nonmagnetostatic calculation with $\omega/k \neq 0$ may also expand the scattering extent in (p, $|\mu|$). In particular, the magnetostatic assumption is less valid for the higher $v_{\rm A}/c$ in our simulations as compared to that of the real ICM. See also Holcomb & Spitkovsky (2019) for further recent discussion.

5. Particle Spectrum from Magnetic Pumping

We now seek a time-integrated view of the energy gain due to magnetic pumping from IC wave scattering during compression. Some particles scatter more efficiently and at different times than others, and it follows that some fossil CRe may gain more energy from magnetic pumping than others.

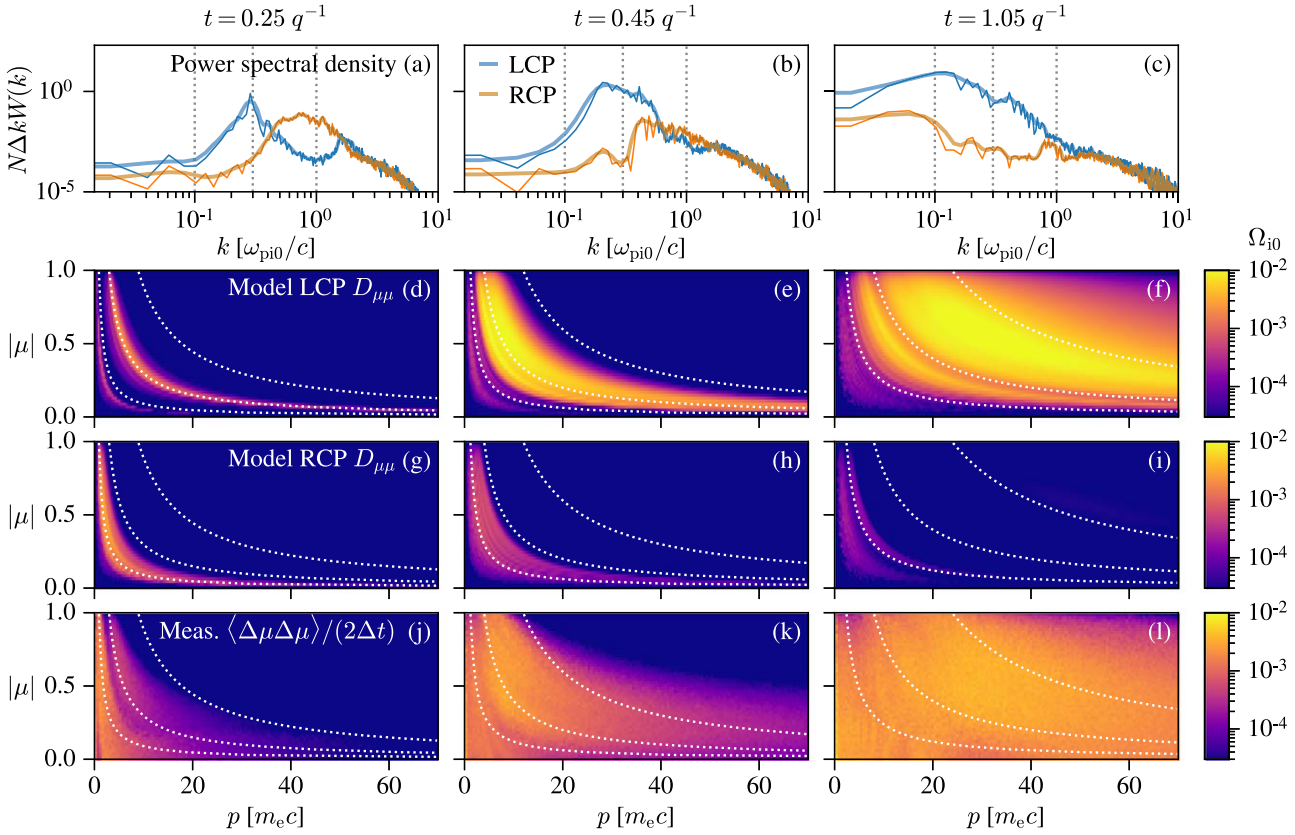

Figure 3. Measured scattering compared to the quasi-linear model at three different times advancing from left to right. (a)–(c) LCP (blue line) and RCP (orange line) magnetic power spectra $W_{\rm L}$ and $W_{\rm R}$. The spectra are normalized using the number of grid points N and the Fourier spacing Δk so that $\int (W_{\rm L} + W_{\rm R})dk = (\delta B_\perp/B_g)^2$. The thick line is the spectrum smoothed with a Hanning window of length $0.14\omega_{\rm pi0}/c$ (7 points), as used to compute $D_{\mu\,\mu}$ in panels (d)–(i) below. (d)–(f) Quasi-linear model for LCP (IC) wave diffusion computed using $W_{\rm L}$. (g)–(i) Quasi-linear model for RCP (whistler) wave diffusion computed using $W_{\rm R}$. (j)–(l) Measured pitch-angle scattering rate $\langle\Delta\mu\Delta\mu\rangle/(2\Delta t)$ for test-particle CRe. White dotted lines mark particles resonant with wavenumbers, from left to right: $k_{\rm res}c/\omega_{\rm pi0} = 1$, 0.3, and 0.1, according to Equation (10); the same wavenumbers are marked as vertical dotted black lines in panels (a)–(c). All scattering rates in panels (d)–(l) are scaled by $\Omega_{\rm i0}$.

To frame the problem, we ask: given CRe of initial momentum p_0 at $t = 0$, what is their energy gain due to magnetic pumping during compression? We consider the following hypothetical scenario. After a compression to time t in our simulation, let the test-particle CRe decompress back to their initial volume, with no further wave scattering during decompression; i.e., map $p_\perp \to p_\perp[B_0/B(t)]^{1/2}$ and hold $p_\parallel$ constant for all particles. We call this adiabatic decompression a "reversion" of the particle distribution, and we say that the particles have undergone a "compress-revert" cycle. The decompressed particle energy is defined as

$$\gamma_{\rm revert}(t) = \sqrt{1 + p_\parallel(t)^2 + p_\perp(t)^2\,[B_0/B(t)]}\,.$$

One cycle of compression to arbitrary time t, followed by a revert, yields an energy gain:

$$\Delta U_{\rm revert} = U_{\rm revert} - U_0 = \langle\gamma_{\rm revert}(t)\rangle - \langle\gamma(t=0)\rangle,$$

where $U(t) = \langle\gamma(t)\rangle$, $U_0 = U(t=0)$, and angle brackets $\langle\cdots\rangle$ are ensemble averages over particles in an initial momentum bin p_0. Recall that our initial test-particle CRe distribution is isotropic; i.e., uniform on $\mu \in [-1, +1]$. We use $\Delta U_{\rm revert}(t)$ as a proxy for magnetic pumping efficiency.

The "revert" is artificial; particles may scatter during decompression. However, the compress-revert cycle permits us to focus solely on magnetic pumping due to compression-driven waves, without needing to also study and separate the effect of decompression-driven waves (e.g., firehose).

We shall now seek to understand how particles respond to a compress-revert cycle, before proceeding to use $\Delta U_{\rm revert}$ as a proxy for magnetic pumping efficiency. In Figures 4–5, we use a test-particle CRe spectrum $dN/dp = f(p) \propto p^{-1}$ that uniformly samples $\log p$ with $p \in [0.0014,\ 1400]m_{\rm e}\ c$ using 14,400,000 particles. However, we reiterate that our results can be reweighted to apply to any initial $f(p)$, and Figure 5 shows one such reweighting to $f(p) \propto p^{-2}$.

Figure 4 shows one compress-revert cycle acting upon the simulated CRe, where the "Final" particle distribution is from the simulation's end, and the "Revert" particle distribution is taken after one compress-revert cycle. The "Final,CGL" distribution shows the same compression as for "Final," but without scattering. We call attention to four points. First, the "Revert" particle spectrum is skewed; although the mean "revert" particle momentum is $\sim$1.1–1.3 $\times\, p_0$, individual particles may be energized up to $\sim$2.4 $\times\, p_0$ (Figures 4(a)–(c)). Second, scattering is strongest for low starting p_0 and weakens toward higher p_0, as judged by the particles' deviation from the predictions for adiabatic compression and adiabatic decompression (Figures 4(d)–(l), black curves). Third, the final particle momentum correlates with the cosine of the particle's

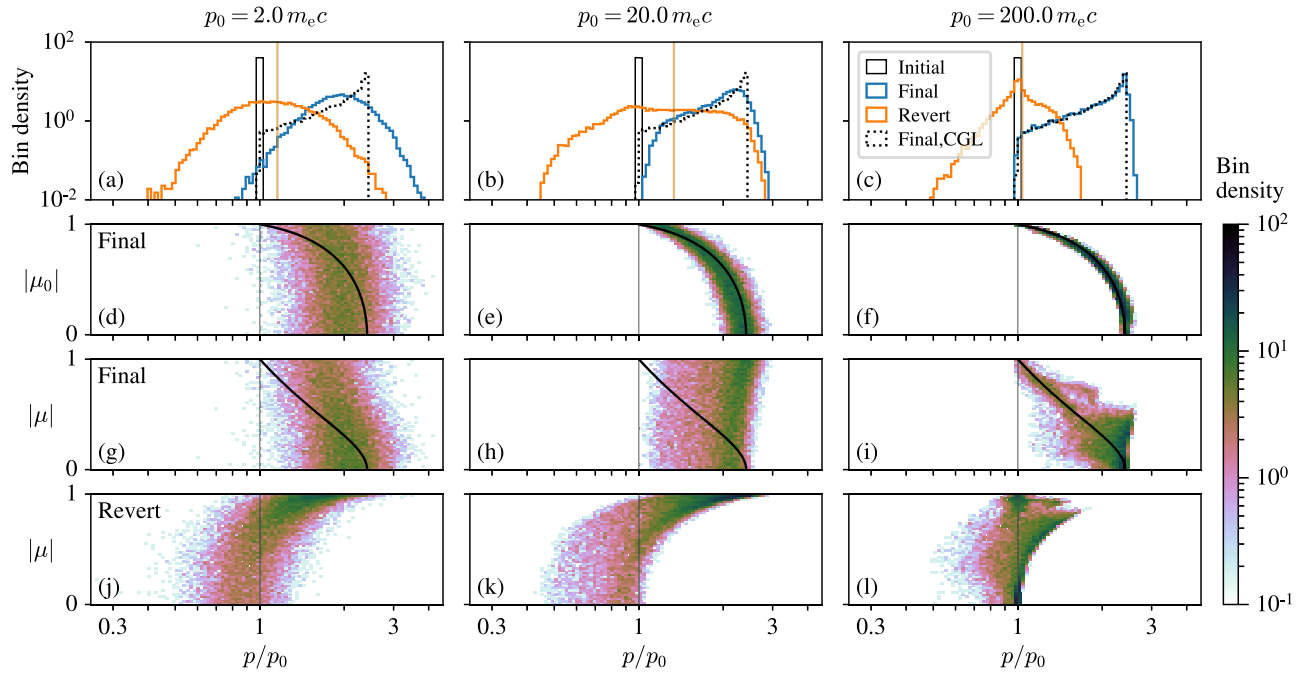

Figure 4. CRe response to compression and adiabatic decompression ("revert") for three narrow initial distributions of mean momentum $p_0 = 2$, 20, $200 m_e\,c$ (left to right), and width $\pm 0.01 p_0$. (a)–(c) 1D CRe spectrum in p at $t = 0$ ("Initial," black), end of simulation ("Final," blue), and after adiabatic decompression ("Revert," orange). For comparison, the CRe spectrum that would result from pure adiabatic compression is "Final, CGL" (dotted black). The mean momentum after the compress-revert cycle is the vertical orange line. (d)–(f) The CRe (p, $|\mu_0|$) distribution shows that the energy gain becomes closer to adiabatic and correlates more with $|\mu_0|$, as p_0 increases. (g)–(i) Final, compressed CRe (p, $|\mu|$) distribution at the end of the simulation. (j)–(l) Revert CRe (p, $|\mu|$) distribution, after a compress-revert cycle. In panels (d)–(l), the vertical black line indicates the starting momentum, and the thick black curve marks the shape of the expected particle distribution for purely adiabatic compression. The histogram bin densities are counts divided by both the 1D/2D bin size and the total count of the particle sample.

initial pitch angle μ_0, and that correlation strengthens for larger p_0 (Figures 4(d)–(f)). The energy gain for particles with large p_0 is nearly consistent with adiabatic compression, shown by comparing the "Final" particle distributions to the "Final,CGL" curve in Figures 4(a)–(c) and thick black curves in Figures 4(d)–(l). Fourth, the "Final" particle distribution extends rightward of the expected maximum momentum from adiabatic compression alone, $p_0\sqrt{B(t)/B_0}$, from comparing the "Final" and "Final,CGL" distributions in Figures 4(a)–(c). We attribute the particles with $p > p_0\sqrt{B(t)/B_0}$ to momentum diffusion D_{pp}; the number of such particles decreases as we lower v_{A0}/c toward realistic values for the ICM and hence decrease D_{pp}.

We can model the magnetic pumping upon any isotropic CRe spectrum $f(p)$ by computing the response of a Dirac-delta distribution $\delta(p - p_0)$ to one compress-revert cycle, for multiple choices of constant p_0, in the spirit of a Green's function. Let p and p' be momentum coordinates before and after a compress-revert cycle, respectively. Define $G(p', p_0)dp'$ as the distribution obtained by applying one compress-revert cycle to an initial distribution $f(p)dp = \delta(p - p_0)dp$ with p_0 being an arbitrary constant, similar to Figures 4(a)–(c). To construct G, we average over μ, even though the particle spectrum after a compress-revert cycle is not isotropic (Figures 4(j)–(l)). Then, the action of one revert cycle upon $f(p)$ is:

$$f_{\rm revert}(p') = \int f(p) G(p', p) dp \tag{11}$$

for any $f(p)$. To numerically implement Equation (11), we compute $G(p', p)$ for each of 300 logarithmically spaced bins over $p \in [0.0014,\ 1400] m_e\,c$ with 96,000 test-particle CRe per bin.

Figure 5 demonstrates the effect of magnetic pumping for an "Initial" spectrum $f(p)dp \propto p^{-2}\,dp$ with lower bound $p = 10^{-0.5}\,m_e\,c$. The "Revert" spectrum $f_{\rm revert}$ has two distinct bumps compared to the Initial spectrum (Figure 5(a)). We attribute the higher-p bump at $p \sim 10$–$100\,m_e\,c$ to the IC wave resonance; hereafter, we call this the "IC bump." The lower-p bump with maximum at $p \sim 1\,m_e\,c$ has shape similar to a thermal Maxwell–Jüttner distribution. At high energies $p \gtrsim 300\,m_e\,c$, particle momenta remain nearly adiabatic through a compress-revert cycle, as previously seen in Figures 4(c), (f), (i), (l). We visualize the convolution of $f(p)$ by plotting the kernels $G(p', p)$ for various p (Figure 5(a)); these kernels are constructed using the same procedure as the 1D "Revert" spectra in Figures 4(a)–(c), up to details of numerical binning and normalization.

The IC bump in $f_{\rm revert}(p)$ has an upper bound at $p \sim 100\,m_e\,c$ that is not exceeded by multiple pump cycles. What sets this p bound? We attribute this bound to the rightward skew of the convolution kernel $G(p', p)$, most visible for the kernels with p between 10^1 and $10^2\,m_e\,c$ in Figure 5(a). In contrast, the mean (μ-averaged) energy gain after one compress-revert cycle has a maximum of $\sim$30% for CRe with initial momenta $p_0 \sim 20$–$30\,m_e\,c$, which we will shortly see in Figure 6; see also the mean energy gain (vertical orange lines) in Figures 4(a)–(c). A mean energy gain of $1.3 \times 30\,m_e\,c$ does not easily explain the increase in $f_{\rm revert}(p)$ at $p \sim 100\,m_e\,c$.

Is the IC bump in $f_{\rm revert}(p)$ sensitive to our choice of the low-p boundary for $f(p)$? Figure 5(b) shows that altering the low-p cutoff on $f(p)$ also alters the amplitude and peak momentum of the thermal bump; i.e., all electrons below $p \sim 1\,m_e\,c$ are reorganized into a thermal distribution. Lowering the p boundary of our input spectrum places more electrons into

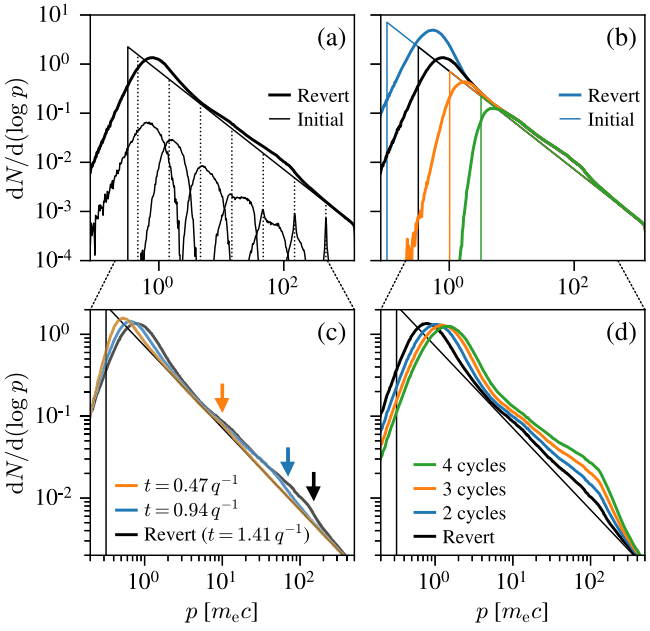

Figure 5. Convolution of an initial CRe spectrum $f(p)dp = p^{-2}\,dp$ with the Dirac-delta spectrum response $G(p', p)$ to one and multiple compress-revert cycles. (a) Initial spectrum $f(p)$ (thin black) and revert spectrum after an assumed adiabatic decompression (thick black). Seven kernels $G(p', p)$ that contribute to the revert spectrum are shown, with their initial p_0 shown by dotted vertical black lines. (b) The low-p bound on $f(p)$ sets the amplitude and position of a thermal bump at $p \sim 1\ m_e\ c$, but does not strongly alter the ion cyclotron (IC) resonance bump at $p \sim 10$–$100\ m_e\ c$. We show four different bounds: $p = 10^{-1}$ (blue), $10^{-0.5}$ (black), 10^{0} (orange), and $10^{0.5}\ m_e\ c$ (green). (c) Compression duration determines the maximum p attained by the IC bump. Here we show f_{revert} from our fiducial spectrum computed at three different times: $t = 0.47q^{-1}$ (orange), $t = 0.94q^{-1}$ (blue), and $t = 1.41q^{-1}$ (black). The black curve is computed at the simulation's end. Corresponding colored arrows indicate the rightward extent of the IC bump in p. (d) Effect of multiple revert cycles, assuming that the spectrum is instantly reisotropized after each revert cycle. In all of panels (a)–(d), the black curve f_{revert} is the same.

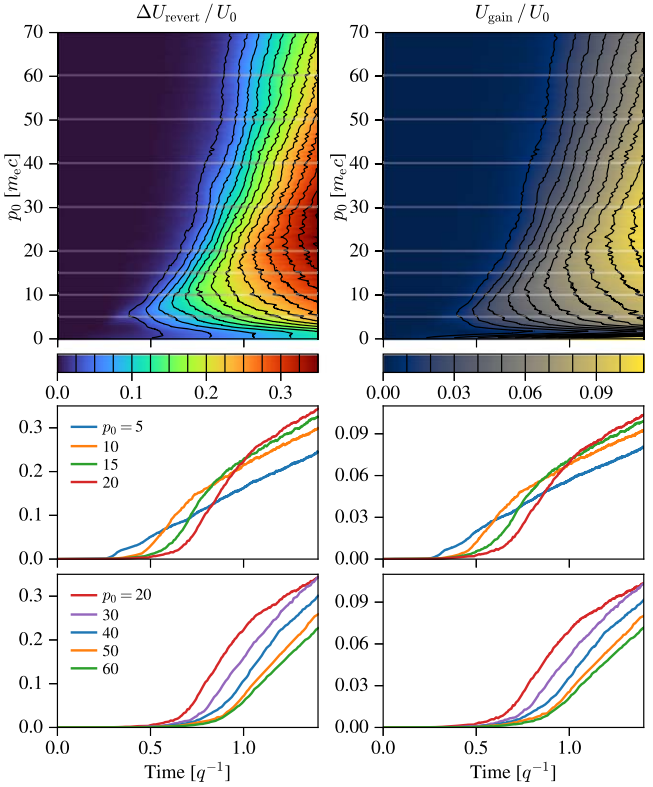

Figure 6. Energy gains $\Delta U_{revert}/U_0$ (left column) and U_{gain}/U_0 (right column), normalized to the initial energy. Top row: energy gain as a function of the CRe initial momentum p_0 and simulation time t, averaged over pitch angle. Middle and bottom rows: 1D slices of the energy gain as a function of time for varying p_0. The horizontal white lines in top row correspond to p_0 selections in the middle and bottom rows.

this thermal bump. The IC bump is not affected by the low-p boundary, which confirms that the thermal and fossil electrons are well separated in momentum space.

The IC bump extends toward higher momenta for longer compression duration. In Figure 5(c) we show f_{revert} computed for three evenly spaced times $t = 0.47$, 0.94, $1.41q^{-1}$ in our fiducial simulation. The spectrum at $t = 0.47q^{-1}$ shows a very weak IC bump, which we attribute to weaker IC scattering at early times when IC waves are not yet saturated. The IC bump becomes more prominent at $t = 0.94q^{-1}$ and $1.41q^{-1}$. We further explore the link between the compression duration and the onset of scattering at high p later in this article.

We also consider the effect of multiple compress-revert cycles by assuming that, at the end of each compress-revert cycle, $f_{revert}(p)$ instantly becomes isotropic in μ; the result is shown in Figure 5(d). Multiple cycles strengthen the IC energy gain between $p = 10$ to $100\ m_e\ c$. The IC pumping does not extend to $p \gg 100\ m_e\ c$; CRe with $p \sim 10^3\ m_e\ c$ remain adiabatic through multiple compress-revert cycles. The assumption of instant isotropization between each compress-revert cycle is questionable; we know from Figures 4(j)–(l) that the revert spectra are far from isotropic. The effect of scattering during decompression, which should bring electrons closer to isotropy, is left for future work.

6. Cumulative Energy Gain from Magnetic Pumping

Let us now focus on the efficiency metric ΔU_{revert}, abstracting away details of the underlying μ-dependent particle spectra. Figure 6 shows $\Delta U_{revert}/U_0$ computed for all test-particle CRe in our simulation, binned by the initial CRe momentum with bin size $\Delta p_0 = 0.5\ m_e\ c$. We emphasize three main features. The lowest-energy CRe, $p_0 \sim 1$–$10\ m_e\ c$, gain little energy from magnetic pumping. The medium-energy CRe, $p_0 \sim 10$–$30\ m_e\ c$, pump the most efficiently by virtue of their having initial momenta at or above the expected resonant $p_\parallel \sim 4$–$25\ m_e\ c$ (Equation (2)). The highest-energy CRe, $p_0 \gtrsim 30\ m_e\ c$, gain energy at later times; as compression proceeds, CRe of progressively higher p_0 "turn on" their energy gain.

We also introduce U_{gain} to represent the time-integrated energy gain from all mechanisms other than adiabatic compression, in particular momentum diffusion. To compute U_{gain}, we decompose each particle's energy gain over a time step Δt into adiabatic and nonadiabatic pieces:

$$\gamma(t + \Delta t) - \gamma(t) = \Delta\gamma_{gain} + \Delta\gamma_{CGL},$$

where γ is the particle's Lorentz factor,

$$\Delta\gamma_{CGL} = \sqrt{1 + p_\parallel(t)^2 + p_\perp(t)^2\,[B(t + \Delta t)/B(t)]} - \gamma(t),$$

and the remaining energy gain is $\Delta\gamma_{\rm gain}$. Then we may time integrate and ensemble average to define

$$U_{\rm gain}(t) = \left\langle \sum_{j=0}^{\lfloor t/\Delta t \rfloor} \Delta\gamma_{\rm gain}(j\Delta t,\, \Delta t) \right\rangle,$$

shown as a function of p_0 and t in Figure 6. The time step $\Delta t = 4.7\Omega_{\rm i0}^{-1}$ matches that used to measure particle scattering in Section 4.

In Figure 6 we draw three conclusions concerning $U_{\rm gain}$. First, both $U_{\rm gain}$ and $\Delta U_{\rm revert}$ show the same qualitative features in $(t,\, p_0)$ coordinates. We attribute this to the shared gyroresonant nature of both energy-gain processes: D_{pp} for nonadiabatic diffusive energization $U_{\rm gain}$, and $D_{\mu\ \mu}$ for magnetic pumping $\Delta U_{\rm revert}$. Second, the magnitude of $U_{\rm gain}$ is $\sim$10% that of the initial particle energy by the end of the simulation; however, $U_{\rm gain}(t)$ is small compared to the total particle energy $U(t)$ arising from compression, which is $\gtrsim$200% of the initial particle energy U_0 by the end of the simulation. Finally, $U_{\rm gain}$ decreases as $v_{\rm A0}/c$ is lowered toward a more realistic value, whereas $\Delta U_{\rm revert}$ does not vary as strongly with $v_{\rm A0}/c$; we show this decrease in $U_{\rm gain}$ later in the article (Figure 12). On the basis of these observations, we view $U_{\rm gain}$ and hence D_{pp} as a minor player in CRe energization through our compressive cycle.

7. Continuous Compression Controls the Efficiency of Magnetic Pumping

The 2D structure of $\Delta U_{\rm revert}(t,\, p_0)$ encodes information regarding which particles scatter and when they scatter; i.e., it encodes the time- and k-dependent wave spectrum $W(k,\, t)$, but we lack a mapping from $W(k,\, t)$ and $B_g(t)$ to $\Delta U_{\rm revert}(t,\, p_0)$. To understand the 2D structure of $\Delta U_{\rm revert}$, we perform Fokker–Planck (F-P) simulations of compression with time-dependent pitch-angle scattering:

$$\frac{\partial f}{\partial t} + \frac{\dot{B}}{B}\frac{p_\perp}{2}\frac{\partial f}{\partial p_\perp} = \frac{\partial}{\partial \mu}\left(D_{\mu\mu}\frac{\partial f}{\partial \mu}\right).$$

We sample 280,000 CRe with momenta between p_0 between 0.25 to 69.75 $m_{\rm e}\,c$ and an isotropic pitch-angle distribution (i.e., uniform $\mu \in [-1, +1]$). Then, we subject the CRe to the same continuous compression as in our fiducial simulation, $B_g(t) = B_0(1 + qt)^2$ with $q^{-1} = 800\Omega_{\rm i0}^{-1}$, using a finite-difference method. Advancing from time t_n to $t_{n+1} = t_n + \Delta t$, each particle's perpendicular momentum is increased adiabatically as $p_\perp(t_{n+1}) = p_\perp(t_n)\sqrt{B_g(t_{n+1})/B_g(t_n)}$; the parallel momentum $p_\parallel(t_{n+1}) = p_\parallel(t_n)$ is held constant. The finite-difference time step $\Delta t = 0.94\Omega_{\rm i0}^{-1}$.

At first, the compression is adiabatic to mimic the relatively weak wave power at early times in our fiducial simulation (Figures 1(a)–(c)). After $t = 0.3q^{-1}$, we begin scattering all particles that satisfy:

$$|k_{\rm res}| = \frac{eB_g(t)}{|\mu|pc} > k_{\rm min}(t), \tag{12}$$

where $k_{\rm min}(t)$ is a user-chosen function. The scattering is implemented as a 1D random walk in pitch angle α. For each time t_n, each particle satisfying Equation (12) takes a randomly signed step $\Delta\alpha = \pm 0.04$ prior to the compression step $p_\perp(t_n) \to p_\perp(t_{n+1})$. The variance of the total displacement after N steps is $\langle\Delta\alpha\Delta\alpha\rangle_{\rm N} = N(\Delta\alpha)^2$, so the effective diffusion coefficient $D_{\mu\ \mu} \sim (1-\mu^2)\langle\Delta\alpha\Delta\alpha\rangle/(2\Delta t)$ is approximately $8.5\times10^{-4}(1-\mu^2)\,\Omega_{\rm i0}$. This $D_{\mu\ \mu}$ value is weaker than the scattering rate measured in our fiducial simulation (Figures 3(j)–(l)); nevertheless, the F-P model returns a comparable value of $\Delta U_{\rm revert}$. Also, our F-P model deviates from quasi-linear theory in having no 90° barrier; particles with $\mu = 0$ scatter efficiently in order to mimic the presence of scattering at $\mu = 0$ in Figures 3(j)–(l). Varying the start time of scattering to either $t = 0.0q^{-1}$ or $0.6q^{-1}$ has only a small effect on the F-P model energy gain; the time evolution of $k_{\rm min}(t)$ is more important.

Figure 7 shows the magnetic-pumping energy gain in our F-P model for four different choices of $k_{\rm min}$. We first consider constant $k_{\rm min} = 0.3$, 0.15, and $0.09\,\omega_{\rm pi0}/c$ in Figures 7(a)–(c). Then, we adopt a time-dependent $k_{\rm min} = k_{\rm IC}(t)$, using Equation (5) to mimic the decreasing-k drift of ion cyclotron wave power in our fiducial PIC simulation. We draw three conclusions. First, the magnetic-pumping energy gain has a self-similar geometric structure in $(t,\, p_0)$ coordinates for $k_{\rm min}$ constant in time; changing $k_{\rm min}$ is the same as rescaling p_0 by a factor $1/k_{\rm min}$ (Equation (12)), so Figures 7(a)–(c) are identical up to linear rescaling along the y-axis. Second, the particles gaining the most energy from magnetic pumping have p_0 somewhat higher than the initial resonant $p_\parallel$ at $t = 0$. For example, choosing $k_{\rm min} = 0.09\omega_{\rm pi0}/c$ gives the most energy to particles with $p_0 \approx 20$–$30\,m_{\rm e}\,c$ (Figure 7(c)), whereas Equation (12) requires $p_\parallel \leqslant 6$–$36\,m_{\rm e}\,c$. Third, the time-dependent $k_{\rm min} = k_{\rm IC}(t)$ broadens the energy-gain "resonance" feature in $\Delta U_{\rm revert}$ toward higher p_0 (Figure 7(d)).

To understand how magnetic pumping interacts with continuously driven compression to "select" a range of p_0 with the highest magnetic pumping efficiency, Figure 8 shows how isotropic, monoenergetic particle distributions with $p_0 = 4$, 12, $36\,m_{\rm e}\,c$ evolve over time while subjected to both compression and pitch-angle scattering (after $t = 0.3q^{-1}$) for all particles with $k_{\rm min} = 0.15\omega_{\rm pi0}/c$ (Figure 7(b)). The lowest-energy particles, $p_0 = 4\,m_{\rm e}\,c$ (blue), scatter promptly at all pitch angles from $t \geqslant 0.3q^{-1}$ onward, so the magnetic pumping is less efficient. The medium-energy particles, $p_0 = 12\,m_{\rm e}\,c$ (orange), only scatter near $\mu = 0$ at early times $t \sim 0.3q^{-1}$, but their scattering extends to most μ values by the simulation's end. The highest-energy particles, $p_0 = 36\,m_{\rm e}\,c$ (green), are mostly adiabatic; few such particles scatter until later times, so their energy gain from magnetic pumping is small.

Preferential scattering near $\mu = 0$, where compression gives the most energy (as compared to larger $|\mu|$), causes medium-energy particles to migrate to large $|\mu|$ and "lock in" their compressive energy gain; therefore, medium-energy particles participate most efficiently in magnetic pumping. We interpret orange particles accumulating at the scattering region boundaries in Figure 8, as well as the skewed particles at large $|\mu|$ in Figures 4(j)–(l), as evidence for energy locking. The highest-energy particles also scatter from $\mu \sim 0$ toward the scattering boundary (Figure 8), but (1) fewer particles are able to participate, and (2) the smaller μ of the scattering boundary causes more compressive energy gain to be removed in decompression. The lowest-energy particles, because they scatter at all μ, easily flow between $\mu \sim 0$ and $|\mu| \sim 1$; there

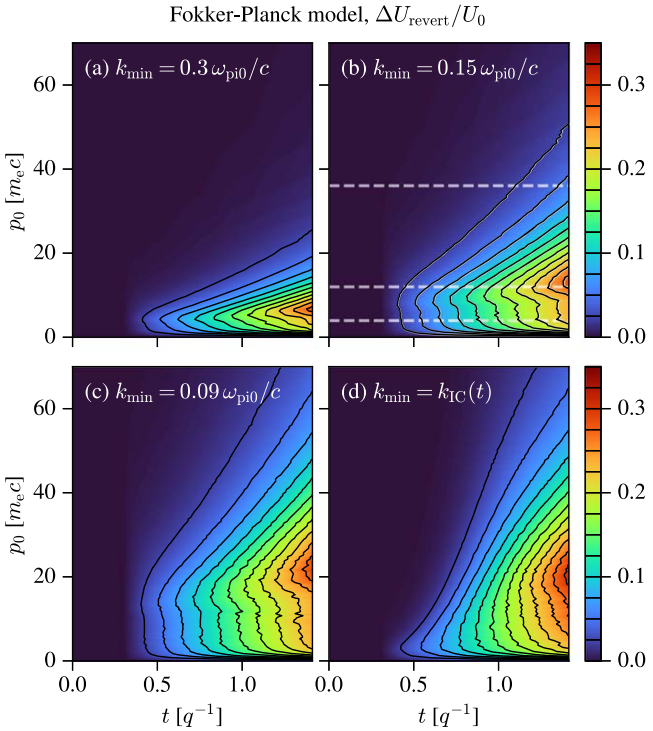

Figure 7. Energy gain from a pure pitch-angle scattering Fokker–Planck (F-P) model, with different prescriptions $k_{\rm min}$ for the particle scattering. Particles compress with the same $B_g(t)$ as that in the fiducial PIC simulation. For $t < 0.3q^{-1}$, no particles scatter; compression is adiabatic. For $t \geqslant 0.3q^{-1}$, particles satisfying Equation (12) scatter by random walk in pitch angle; see the text for details. (a)–(c) Time-constant $k_{\rm min} = 0.3$, 0.15, and $0.09\,\omega_{\rm pi0}/c$. (d) Time-dependent $k_{\rm min} = k_{\rm IC}(t)$ (Equation (5)) mimicking the decreasing-k drift of ion cyclotron wave power seen in our fiducial PIC simulation. The dashed white lines in (b) correspond to the particle samples in Figure 8.

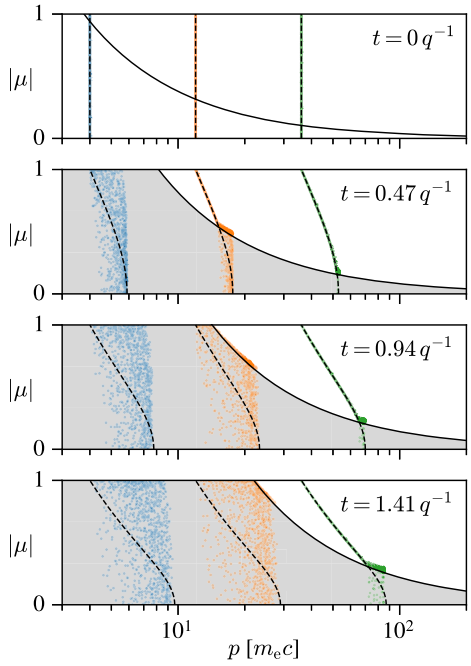

Figure 8. Evolution of initially isotropic, monoenergetic particle distributions with $p_0 = 4$, 12, 36 in the F-P scattering model with $k_{\rm min} = 0.15\,\omega_{\rm pi0}/c$, corresponding to Figure 7(b). The black solid curves show the bounds of Equation (12); particles scatter within the bounded, gray-shaded region and evolve adiabatically otherwise. The black dashed lines mark curves upon which particles would evolve from p_0 if there were no scattering at all.

is no region of $(p, |\mu|)$ space in which particles may lock energy gained from $\mu \sim 0$.

The drift of IC power toward low k further modifies particle energization. In Figure 8, the gray scattering region expands rightward as time progresses: $p_\parallel \propto B_g(t)/k_{\rm res}$, and $k_{\rm res}$ decreasing in time will hasten that expansion and therefore widen the band of medium-energy particles. Previously, Matsukiyo & Hada (2009, Section 4) have also noted how Alfvénic waves drifting to low k may help accelerate particles that can stay within the range of resonant momenta of the time-evolving waves.

Compression and the drift of IC power toward low k together can thus explain, qualitatively, the distinct low-, medium-, and high-energy CRe structure of $\Delta U_{\rm revert}$ as a function of t and p_0 (Figure 6).

8. Compression Rate Dependence

In our simulations, the compression timescale $q^{-1} = 800\,\Omega_{\rm i0}^{-1}$ corresponds to $q^{-1} \sim 10^{-3}$ yr if one assumes $B_0 = 3\,\mu$G, which is much smaller than the actual sound-crossing time $\sim 10^8$ yr for cluster-scale ICM bulk motion. How do the CRe energy gain and the IC wave spectrum change with q^{-1} in our simulations? For larger q^{-1}, linearly unstable IC waves grow earlier and attain smaller k at late times (Figure 9), so we expect the IC wave resonance to broaden toward higher p.

We also expect the wave power $\delta B_\perp^2$ to weaken for larger q^{-1} as per Equation (7), which may be rewritten more explicitly as

$$\left(\frac{\delta B_\perp}{B_g}\right)^2 \frac{\Delta_{\rm i}(2\Delta_{\rm i}+3)}{\Delta_{\rm i}+1} \propto \frac{2q/\Omega_{\rm i0}}{(1+qt)^3}. \tag{13}$$

In Figure 10, we check if the linear scaling with q predicted by Equation (13) holds in our simulations. Both $(\delta B_\perp/B_g)^2$ and $\Delta_{\rm i}$ decrease when q decreases (Figures 10(a)–(b)). At $t = 1.2q^{-1}$, we sample and plot $(\delta B_\perp/B_g)^2$ as a function of q (Figure 10(c), solid markers). We similarly compute and plot the left-hand side (LHS) of Equation (13) (Figure 10(c), hollow markers). Both quantities appear to follow a power-law scaling q^n with exponent $n \lesssim 0.5$, which is a weaker proportionality than that predicted by Equation (13).

Waves at differing k may not contribute equally toward balancing the compression-driven anisotropy; recall how the strongest waves lie outside the unstable ω range in Figure 1(a), and how Equation (7) agrees better with the unstable wave power rather than the total wave power in Figure 1(c). We thus suspect that low-frequency wave power may participate less in regulating the ion anisotropy. Does the anisotropy-driven high-frequency wave power, rather than the total wave power, scale linearly with q as per Equation (13)? We select wave power with $\omega/\Omega_{\rm i0} > 0.9$ by computing the average wave power spectral density (PSD) in the top-right white boxes of Figures 9(a)–(e);[7] the resulting PSD is plotted against q in Figure 10(d). The PSD multiplied by $\Delta_{\rm i}(2\Delta_{\rm i}+3)/(\Delta_{\rm i}+1)$ appears to follow a power-law scaling q^n with exponent n between 0.5 and 1.

[7] The PSD averaged in Fourier space equals the real-space average of $(\delta B_\perp/B_g)^2$ (i.e., an ω-average of Figures 9(a)–(e) or a k-average of Figures 9(f)–(j) will return the domain-averaged wave power in Figure 10(a)).

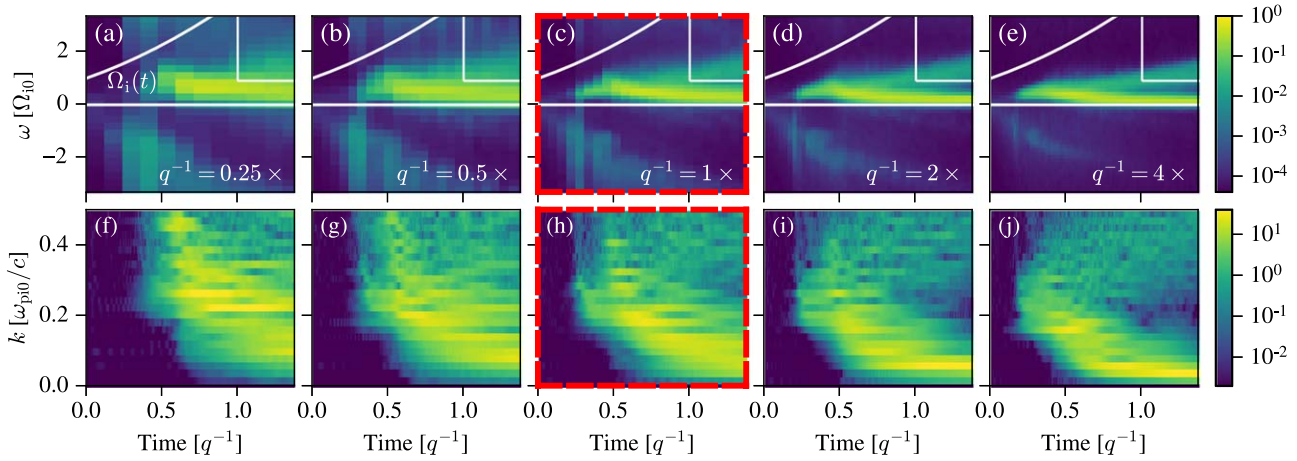

Figure 9. Wave power spectrogram of $B_z + iB_x$ for varying q, from small q^{-1}/fast compression (left) to large q^{-1}/slow compression (right). (a)–(e) Spectrogram in (t, ω) coordinates with a finite time binning for each pixel. The white curve on the top left of each panel is $\Omega_i(t)$. Within the white boxes ($t > 1q^{-1}$ and $\omega/\Omega_{i0} > 0.9$), we average the PSD to estimate the power due to unstable IC waves at high ω, omitting the linearly stable IC waves at low ω. (f)–(j) Wave power spectrum in (t, k) coordinates without time binning. The red-dash-framed panels (c), (h) mark the fiducial simulation; i.e., same data as Figure 1.

Least-squares fits of form $A(q/\Omega_{i0})^n$, with free parameters A and n, are plotted as solid black lines in Figures 10(c)–(d). For Equation (13) LHS (Figure 10(c), hollow squares), and $\delta B_\perp{}^2$ (Figure 10(c), solid circles), we obtain $n = 0.48 \pm 0.02$ and 0.32 ± 0.02, respectively. For the high-frequency wave PSD replacing $\delta B_\perp{}^2$ in Equation (13) LHS (Figure 10(d), hollow squares), and the high-frequency wave PSD alone (Figure 10(d), solid circles), we obtain $n = 0.69 \pm 0.05$ and 0.54 ± 0.07, respectively. We fit the data in log coordinates (i.e., linear regression). The uncertainty on n is one standard deviation estimated by assuming $\chi^2_{\rm reduced} = 1$, as no data uncertainty is used in fitting. We expect that the systematic uncertainty is larger.

We warn that our $\omega/\Omega_{i0} > 0.9$ threshold does not cleanly separate low- and high-frequency wave power for every simulation because the ω range of the wave power varies with q (Figure 9). Altering the ω threshold will also alter the q-scaling exponent in Figure 10(d). A multicomponent fit to the power spectrum may better separate the low- and high-frequency wave power and so provide a better test of Equation (7), but we omit such detailed modeling for now.

We also show how the CRe energy gain $\Delta U_{\rm revert}$ changes with q in Figure 11. As q^{-1} increases, the optimal p_0 range for magnetic pumping both widens and moves to higher momenta, which we ascribe to both the lower late-time k and earlier onset of waves with respect to the compression timescale q^{-1}. We suspect that wave evolution toward lower k is the dominant effect altering the shape of $\Delta U_{\rm revert}$ for varying q^{-1}. We do not observe, by eye, a trend in the peak magnitude of $\Delta U_{\rm revert}$ with respect to q.

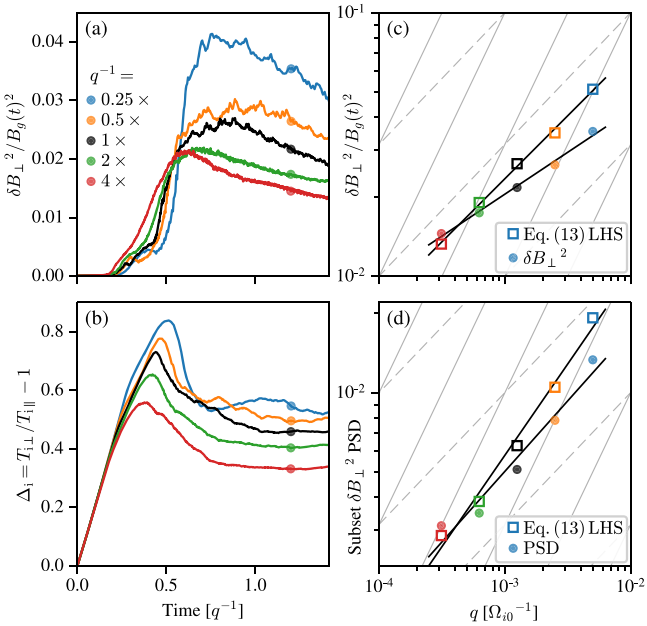

Figure 10. Scaling of $\delta B_\perp{}^2/B_g(t)^2$ power from simulations with varying q, indicated by the marker/line color. (a) Wave power $\delta B_\perp{}^2/B_g(t)^2$ over time, domain-averaged. (b) Ion temperature anisotropy $\Delta_i = T_{i\perp}/T_{i\parallel} - 1$ over time t. (c) Wave power at $t = 1.2\,q^{-1}$ plotted as a function of q (solid circles). The same wave power is multiplied by $\Delta_i(2\Delta_i + 3))(\Delta_i + 1)$, i.e., the left-hand side (LHS) of Equation (13) (hollow squares), to test the linear q scaling of Equation (13). The solid, dashed light-gray lines are $\propto q$, $\sqrt{q}$ scalings, respectively. The solid black lines are least-squares power-law fits. (d) Like (c), but replace $\delta B_\perp{}^2/B_g(t)^2$ with time-averaged PSD sampled from white-boxed subsets of the spectrograms in Figures 9(a)–(e); see the text for details.

9. Scaling to Realistic ICM Plasma Parameters

How do more realistic simulation parameters (higher m_i/m_e, lower v_A/c) alter our results? Let us define a dimensionless CRe momentum

$$\tilde{p} \propto p\left(\frac{m_i}{m_e}\right)^{-1}\left(\frac{v_{A0}}{c}\right)^{-1}$$

with the constraint $\tilde{p} = p$ for our fiducial simulation parameters, motivated by the gyroresonance scaling (Equation (2)); recall that $v_{th,i}/c \propto v_A/c$ for fixed β_p. As in Sections 5–6, $\tilde{p}_0$ is the value of $\tilde{p}$ for CRe particles at $t = 0$. If simulations of varying v_{A0}/c and m_i/m_e have a similar IC wave spectrum $W(t, k)$ for fixed q/Ω_{i0}, then particle scattering and energization should also have a similar structure in $\tilde{p}$.

We vary v_{A0}/c of our fiducial simulation by factors of $\sqrt{2}$ and measure the particle scattering rates $\langle \Delta p \Delta p/p^2 \rangle/(2\Delta t)$ and $\langle \Delta\mu\Delta\mu \rangle/(2\Delta t)$ in discrete (p, μ) bins. As in Section 4, the time step is $\Delta t \approx 5\Omega_{i0}^{-1}$. The momentum bin width $0.5 m_e\, c$ is fixed

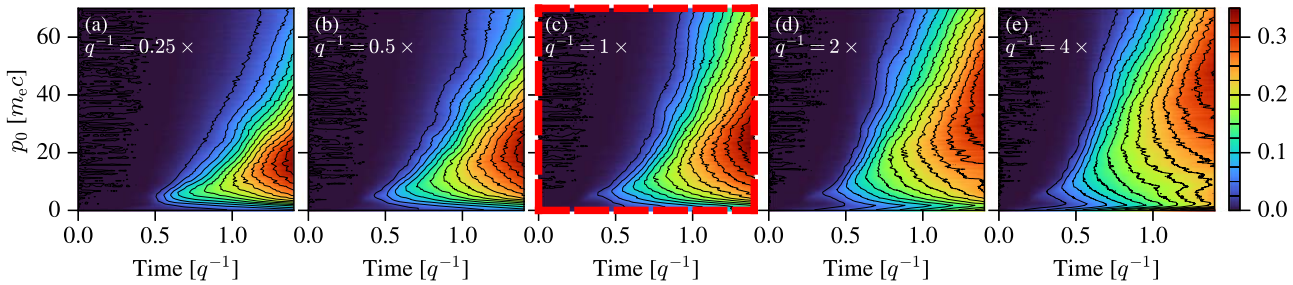

Figure 11. Energy-gain metric $\Delta U_{\rm revert}/U_0$, showing the effect of (a) faster $q^{-1} = 200\ \Omega_{\rm i0}^{-1}$ to (e) slower $q^{-1} = 3200\ \Omega_{\rm i0}^{-1}$ compression upon CRe energization. The red-dash-framed panel (c) is the fiducial simulation, same as Figure 6.

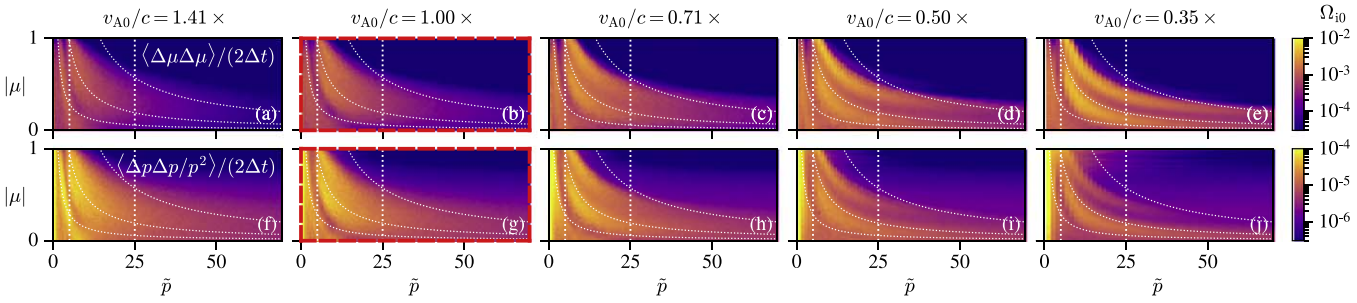

Figure 12. Scattering rates measured at $t = 0.35q^{-1}$ in simulations of varying $v_{\rm A0}/c$, decreasing left to right. (a)–(e) Pitch-angle scattering $\langle\Delta\mu\Delta\mu\rangle/(2\Delta t)$. (f)–(j) Momentum scattering $\langle\Delta p\Delta p/p^2\rangle/(2\Delta t)$. The white dotted vertical lines mark the averaging region used in Figure 13. The white dotted curves are the same contours of the constant resonant wavenumber as those in Figure 3. The red-dash-framed panels (b), (g) mark the fiducial simulation. All rates are in units of $\Omega_{\rm i0}$.

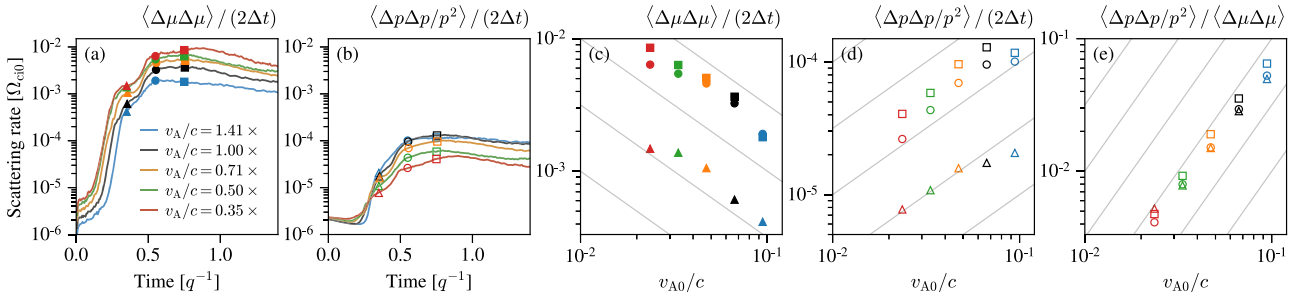

Figure 13. (a)–(b) Scattering rates $\langle\Delta\mu\Delta\mu\rangle/(2\Delta t)$ and $\langle\Delta p\Delta p/p^2\rangle/(2\Delta t)$ measured in five simulations with varying $v_{\rm A0}/c$ (line/marker color), reported in units of $\Omega_{\rm i0}$. The rates are averages over the $(\tilde{p}, |\mu|)$ regions marked in Figure 12. (c)–(d) Sample points from (a)–(b) plotted as a function of $v_{\rm A0}/c$. Light-gray lines show $(v_{\rm A}/c)^{-1}$ (panel (c)) and $(v_{\rm A}/c)^{+1}$ (panel (d)) scalings. (e) Ratio of p and μ scattering rates. Light-gray lines show $(v_{\rm A}/c)^2$ (panel (e)) scaling. In all panels, symbols correspond to different times at which the scattering rates are measured.

for all simulations, so the plotted $\tilde{p}$ bin width varies between simulations in Figure 12.

The measured scattering rates indeed have similar shape in $(\tilde{p}, |\mu|)$ coordinates for varying $v_{\rm A0}/c$ (Figure 12). At lower $v_{\rm A0}/c$, a double-lobed scattering region appears along the resonant contours. Lower $v_{\rm A0}/c$ also alters the apparent edge of the scattering region at $\tilde{p} > 25$ toward possibly better agreement with the predicted resonant contours from Equation (10), although the scattering region edge still disagrees at low $\tilde{p} < 25$.

To explore how scattering scales with $v_{\rm A0}/c$, we average the scattering rates over $|\mu|$ and $\tilde{p} \in [5, 25] m_e c$ to sample the strongest IC wave signal in momentum space. The average rates are plotted as a function of time in Figures 13(a)–(b); the same rates sampled at three discrete times are then plotted as a function of $v_{\rm A0}/c$ in Figures 13(c)–(d). The pitch-angle and momentum scattering rates increase and decrease, respectively, as $v_{\rm A0}/c$ decreases. We interpret the data as showing a transition from mildly relativistic to nonrelativistic behavior as we lower $v_{\rm A0}/c$. At lower $v_{\rm A0}/c$ than shown, we expect that the pitch-angle scattering should become independent of $v_{\rm A0}/c$, while momentum scattering should scale as $(v_{\rm A0}/c)^2$. We also verify the expected QLT scaling:

$$\frac{\langle\Delta p\Delta p/p^2\rangle}{\langle\Delta\mu\Delta\mu\rangle} \propto \left(\frac{v_{\rm A}}{c}\right)^2$$

in Figure 13(e), which shows a power-law-like scaling consistent through the entire range of $v_{\rm A0}/c$ considered.

As previously claimed, momentum scattering is not important in a single compress-revert cycle for our simulation parameters. We see that $\langle\Delta p\Delta p/p^2\rangle/(2\Delta t)$ is $\sim 10^{-2}\times$ smaller than $\langle\Delta\mu\Delta\mu\rangle/(2\Delta t)$, and the QLT scaling assures us that momentum scattering is even less important in real ICM with $v_{\rm A}/c \lesssim 10^{-3}$. In Figure 13(e), the separation between data measured at different times in the same simulation may be partly attributed to time variation in $v_{\rm A}(t)/c$.

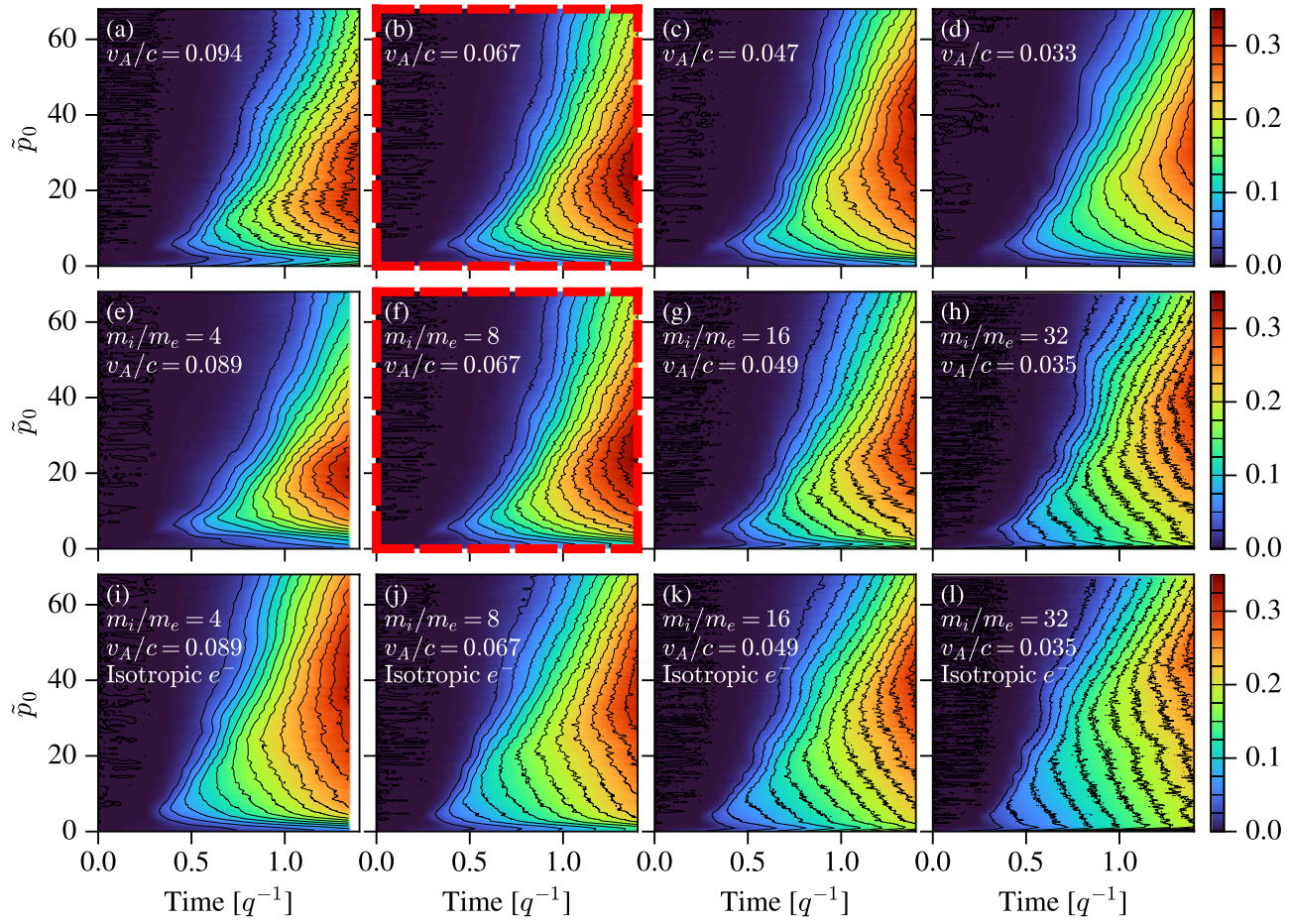

Figure 14. Energy-gain metric $\Delta U_{\rm revert}/U_0$, like Figure 6 but with $\tilde{p}_0$ rather than p_0 on the y-axis, for simulations of varying $v_{\rm A0}/c$ and $m_{\rm i}/m_{\rm e}$. (a)–(d) Varying $v_{\rm A0}/c$ with fixed $m_{\rm i}/m_{\rm e} = 8$. (e)–(h) Varying $m_{\rm i}/m_{\rm e}$ and $v_{\rm A}/c$ together, to help understand the effect of $m_{\rm i}/m_{\rm e}$. (i)–(l) Like panels (e)–(h), but disabling whistler waves by compressing electrons isotropically at the rate $q_{\rm iso} = 2q/3$. The red-dash framed panels (b), (f) are the fiducial simulation, previously shown in Figure 6.

We proceed to vary $m_{\rm i}/m_{\rm e}$ and $v_{\rm A0}/c$ together, now focusing solely on the magnetic pumping efficiency $\Delta U_{\rm revert}$, in Figure 14. Across all panels, we observe a similar three-band structure as in our fiducial simulation: low-energy CRe ($\tilde{p}_0 \lesssim 5$) gain little energy, medium-energy CRe ($\tilde{p}_0 = 10$–30) gain the most energy, and high-energy CRe ($\tilde{p}_0 \gtrsim 30$) progressively "turn on" their energy gain over time, later for higher-energy CRe. If we remove whistler waves by compressing electrons isotropically (Section 2), comparing Figures 14(e)–(h) against Figures 14(i)–(l): the region of the most efficient energy gain shifts to higher $\tilde{p}_0$, and the maximum value of $\Delta U_{\rm revert}/U_0$ decreases in magnitude by $\sim$0.05. Otherwise, the overall shape of $\Delta U_{\rm revert}$ remains similar when comparing simulations with and without whistler waves.

10. Conclusions and Outlook

We have used 1D PIC simulations to show how ICM fossil CRe gain energy from bulk compression by scattering upon IC waves excited by anisotropic thermal ions. The energy gain comes from magnetic pumping, and we have measured the momentum-dependent pumping efficiency. Some summary points follow. First, high-$\beta_{\rm p}$ plasma microinstabilities have a convenient wavelength—comparable to the Larmor radius of thermal protons—to interact with and scatter fossil CRe in the ICM of galaxy clusters. Second, continuous compression and wave-power drift toward low k both increase, over time, the CRe momentum p that can resonantly scatter on IC waves and hence gain energy via magnetic pumping. The increase in the resonant p may be viewed as a time-delayed scattering for high-p CRe, which can help increase the pumping energy gain compared to continuous scattering from beginning to end of the simulation. Third, IC wave pumping is robust with respect to $m_{\rm i}/m_{\rm e}$ and $v_{\rm A0}/c$ and is not sensitive to the presence or absence of whistler waves driven by thermal electrons. Although the simulated $m_{\rm i}/m_{\rm e}$ and $v_{\rm A0}/c$ are not realistic, the lower $m_{\rm i}/m_{\rm e}$ and higher $v_{\rm A0}/c$ cancel such that the simulated resonant momenta are only 2–3$\times$ lower than those of real fossil CRe.

Our 1D setup with an adiabatic "revert" is unrealistic in some ways. The compression factor $\sim$6 at the end of our simulation exceeds the expected density contrast of both weak ICM shocks and subsonic compressive ICM turbulence (e.g., Gaspari & Churazov 2013). More realistic, nonadiabatic decompression may excite firehose modes that should also resonantly scatter CRe and alter $\Delta U_{\rm revert}$ (Melville et al. 2016; Riquelme et al. 2018; Ley et al. 2023). In 2D or 3D simulations, the low-k drift of IC wave power may not persist, and mirror modes may weaken IC waves; both effects will weaken the energy gain from IC wave pumping. Nevertheless,

magnetic pumping via resonant scattering on firehose fluctuations or nonresonant scattering on mirror modes remains possible, as both firehose and mirror modes will also have a convenient wavelength to interact with fossil CRe. Varying $|\boldsymbol{B}|$ in solenoidal, shear-deforming flows will also excite the same high-β_p plasma microinstabilities to scatter and magnetically pump CRe.

Our treatment of a collisionless ion–electron plasma has neglected (1) Coulomb collisions and (2) the presence of heavier ions. Regarding (1), the collision rate varies within a cluster. The ICM density decreases to $\sim 10^{-5}$–$10^{-4}\,\mathrm{cm}^{-3}$ at large radii from cluster centers, and the proton collision time can reach $\gtrsim$100 Myr, comparable to the sound-crossing time as discussed in Section 8. In denser gas closer to cluster centers, collisions may inhibit large-scale eddies from driving particle anisotropy. However, we expect that the turbulent cascade will eventually reach an eddy scale where the turnover rate is faster than the collision rate, so that particle anisotropy may be collisionlessly driven. Regarding (2), He and heavier ions are known to exist in the ICM (Abramopoulos et al. 1981; Peng & Nagai 2009; Berlok & Pessah 2015; Mernier et al. 2018). He++ and other ions will modify the parallel plasma dispersion relation (Smith & Brice 1964) and proton cyclotron instability growth rate (Gary et al. 1993), and He++ cyclotron waves may themselves be excited (Gary et al. 1994a). Mirror and firehose linear instability thresholds will be altered as well (Hellinger 2007; Chen et al. 2016). The precise wave spectrum and hence CRe energy gain would thus change, but we expect that CRe may still gain energy by magnetic pumping in the presence of heavier ICM ions.

How does CRe energization by high-β_p IC wave magnetic pumping fit into the broader context of large-scale ICM flows and turbulence? At ion Larmor scales, we expect power from high-β_p plasma microinstabilities to be much larger than power from the direct turbulent cascade. Let us suppose that the ICM has a turbulent magnetic energy spectrum:

$$\left\langle \frac{B^2}{8\pi} \right\rangle = \frac{1}{V}\int \frac{B^2}{8\pi} dV = \int_{2\pi/L}^{\infty} W_{\rm turb}(k)\,dk \propto \int k^{-n} dk$$

with outer scale L and $n = 5/3$ for a Kolmogorov cascade. The energy at the ion (proton) Larmor wavenumber $k_i = 2\pi/\rho_i$ may be estimated as (Kulsrud & Pearce 1969):

$$\frac{k_i W_{\rm turb}(k_i)}{\langle B^2/(8\pi)\rangle} = (n-1)\left(\frac{L}{\rho_i}\right)^{-n+1} \approx 6.7\times 10^{-11} \qquad (14)$$

for ICM parameters $L = 1$ Mpc and $\rho_i = 1$ npc. For comparison, our fiducial simulation has:

$$\frac{k_i W_{\rm PIC}(k_i)}{{B_g}^2/(8\pi)} \approx 5.1\times 10^{-3}. \qquad (15)$$

We suppose that the simulated B_g^2 corresponds to the total magnetic energy $\langle B^2\rangle$ in the ICM, because energy resides at the largest scales in the Kolmogorov spectrum.

Let us further consider IC waves driven by a compressive eddy at a galaxy cluster's outer scale, $\sim$1 Mpc. Using the estimate from the beginning of Section 8, the compression timescale q^{-1} will be $10^{11}\times$ larger than in our simulation. Combined with the scaling $\delta B_\perp^2 \propto q^{0.32}$ from Figure 10(c), we should decrease our estimate of $k_i\,W_{\rm PIC}(k_i)$ in Equation (15) by a factor of 3×10^3 in order to extrapolate to realistic conditions. The IC wave power so extrapolated remains 10^5 times larger than the power expected from the turbulent direct cascade at ion Larmor scales.

The excess power at ion Larmor scales may also contribute to stochastic reacceleration via momentum scattering (D_{pp}), as explored for Alfvénic cascades by Blasi (2000) and Brunetti et al. (2004). Let us suppose that $D_{pp} \propto (v_A/c)^2 q^{0.32}$, from Figure 13 and its accompanying discussion. Again, we take the ICM outer scale $q^{-1} \sim 10^{11}\times$ larger than our simulation, and also take ICM $v_A/c \sim 10^{-3}$ and $\Omega_i^{-1} \sim 10^{-6}$ yr. Our measured momentum scattering rate $10^{-4}\,\Omega_i$ (Figure 13) then extrapolates to $\langle \Delta p \Delta p/p^2\rangle/(2\Delta t) \sim 10^{-11}\,\Omega_i$. The corresponding acceleration time $\sim 10^5$ yr is short compared to cosmological timescales.

What is the efficiency of magnetic pumping, as well as stochastic reacceleration, upon IC waves in this slowly forced, turbulent setting? A quantitative answer is beyond the scope of this work, but we make a few remarks. For CRe momenta within the band of IC wave resonance, scattering will occur quickly and persist throughout the bulk compression. Both resonant magnetic pumping and stochastic reacceleration will be limited by the available IC wave bandwidth, so electrons will not reach arbitrarily high energies. If the IC wave drift rate toward low k scales with Ω_i rather than q, owing to the smaller q in reality, wave energy may continue to cascade to smaller k than in our simulations and so help scatter and pump CRe at even higher momenta. At galaxy cluster merger shocks, nonthermal protons may also alter the growth and damping of IC waves and hence their resulting bandwidth (e.g., dos Santos et al. 2015). In a turbulent flow, the microinstabilities will not be volume filling; CRe streaming in and out of the scattering regions may also alter the energy gain from magnetic pumping (Egedal & Lichko 2021; Egedal et al. 2021).

We are very grateful for discussions with Luca Comisso, Daniel Grošelj, Kris Klein, and Navin Sridhar. We thank the anonymous referee for thoughtful comments and suggestions. A.T. and L.S. were partly supported by NASA ATP 80NSSC20K0565. A.T. was partly supported by NASA FINESST 80NSSC21K1383. F.L. and E.G.Z. were supported by NSF PHY 2010189. M.A.R. thanks support from ANID Fondecyt Regular grant No. 1191673. Simulations and analysis used the computer clusters Habanero, Terremoto, Ginsburg (Columbia University), and Pleiades (NASA). Computing resources were provided by Columbia University's Shared Research Computing Facility (SRCF) and the NASA High-End Computing Program through the NASA Advanced Supercomputing (NAS) Division at Ames Research Center. Columbia University's SRCF is supported by NIH Research Facility Improvement Grant 1G20RR030893-01 and the New York State Empire State Development, Division of Science Technology and Innovation (NYSTAR) Contract C090171.

Facility: Pleiades.

Appendix A
Drift-kinetic Moment Equations

Here we derive Equation (6) from a set of moment equations, similar to the drift-kinetic models of Zweibel (2020) and Ley et al. (2023); a more general form is given by Chew et al.

(1956, Equations (31)–(32)). Assuming gyrotropy, compression perpendicular to $\boldsymbol{B}$, and Lorentz pitch-angle scattering with rate ν constant over momentum and pitch angle, the relativistic Vlasov equation is

$$\frac{\partial f}{\partial t} + \frac{\dot{B}}{B}\frac{p_\perp}{2}\frac{\partial f}{\partial p_\perp} = \frac{\partial}{\partial \mu}\left(\frac{\nu(1-\mu^2)}{2}\frac{\partial f}{\partial \mu}\right), \tag{A1}$$

where v is normalized to c, p is normalized to mc, and m is either the ion or electron mass, depending on the species of interest. Let us compute the evolution equations for the moments $P_\perp = \langle p_\perp\ v_\perp/2\rangle$ and $P_\parallel = \langle p_\parallel\ v_\parallel\rangle$, where $\langle\chi\rangle = \int \chi\, f d^3\,\boldsymbol{p}$, by multiplying Equation (A1) by $p_\perp\, v_\perp/2$ and $p_\parallel\, v_\parallel$. For $P_\perp$, we have:

$$\begin{aligned}\frac{dP_\perp}{dt} &= -\frac{\dot{B}}{B}\int \frac{1}{4}p_\perp^2 v_\perp \frac{\partial f}{\partial p_\perp} 2\pi p_\perp dp_\perp dp_\parallel - \nu(P_\perp - P_\parallel)\\ &= \frac{\dot{B}}{B}\left\langle \frac{1}{2}p_\perp v_\perp\left(2 - \frac{1}{2}v_\perp^2\right)\right\rangle - \nu(P_\perp - P_\parallel).\end{aligned}$$

Similarly for $P_\parallel$, we have:

$$\begin{aligned}\frac{dP_\parallel}{dt} &= -\frac{\dot{B}}{B}\int p_\parallel v_\parallel \frac{p_\perp}{2}\frac{\partial f}{\partial p_\perp} 2\pi p_\perp dp_\perp dp_\parallel + 2\nu(P_\perp - P_\parallel)\\ &= \frac{\dot{B}}{B}\left\langle p_\parallel v_\parallel\left(1 - \frac{1}{2}{v_\perp}^2\right)\right\rangle + 2\nu(P_\perp - P_\parallel).\end{aligned}$$

In the nonrelativistic limit,

$$\begin{aligned}\frac{dP_\perp}{dt} &= \frac{\dot{B}}{B}2P_\perp - \nu(P_\perp - P_\parallel)\\ \frac{dP_\parallel}{dt} &= \frac{\dot{B}}{B}P_\parallel + 2\nu(P_\perp - P_\parallel),\end{aligned}$$

which we then use to obtain Equation (6).

Appendix B
Whistler-mode Offset from Bi-Maxwellian Dispersion

What causes the RCP mode offset discussed in Section 3.2? Though we do not yet know, we checked how it behaves in varying plasma conditions. The offset mode must come from free energy in electron temperature anisotropy flowing into the whistler branch, and the offset requires hot ions, based on several simulations shown in Figure 15. If we compress electrons isotropically, the offset mode disappears, whereas if we compress ions isotropically, the offset mode persists (Figures 15(b)–(c)). The offset persists at higher $\beta_{\rm p0} = 63$ and disappears at lower $\beta_{\rm p0} = 6.3$ and $\beta_{\rm p0} = 2$, with $T_{\rm i0} = T_{\rm e0}$ for all $\beta_{\rm p0}$ values (Figures 15(d)–(f)). The offset mode persists at larger q^{-1} and lower $v_{\rm A0}/c$, i.e., toward more realistic ICM conditions (Figures 15(g)–(h)). Further, the offset mode persists at $m_{\rm i}/m_{\rm e} = 32$; the location and the bandwidth of the mode power in (ω, k) space follows the whistler branch rather than the IC branch (Figure 15(i)).

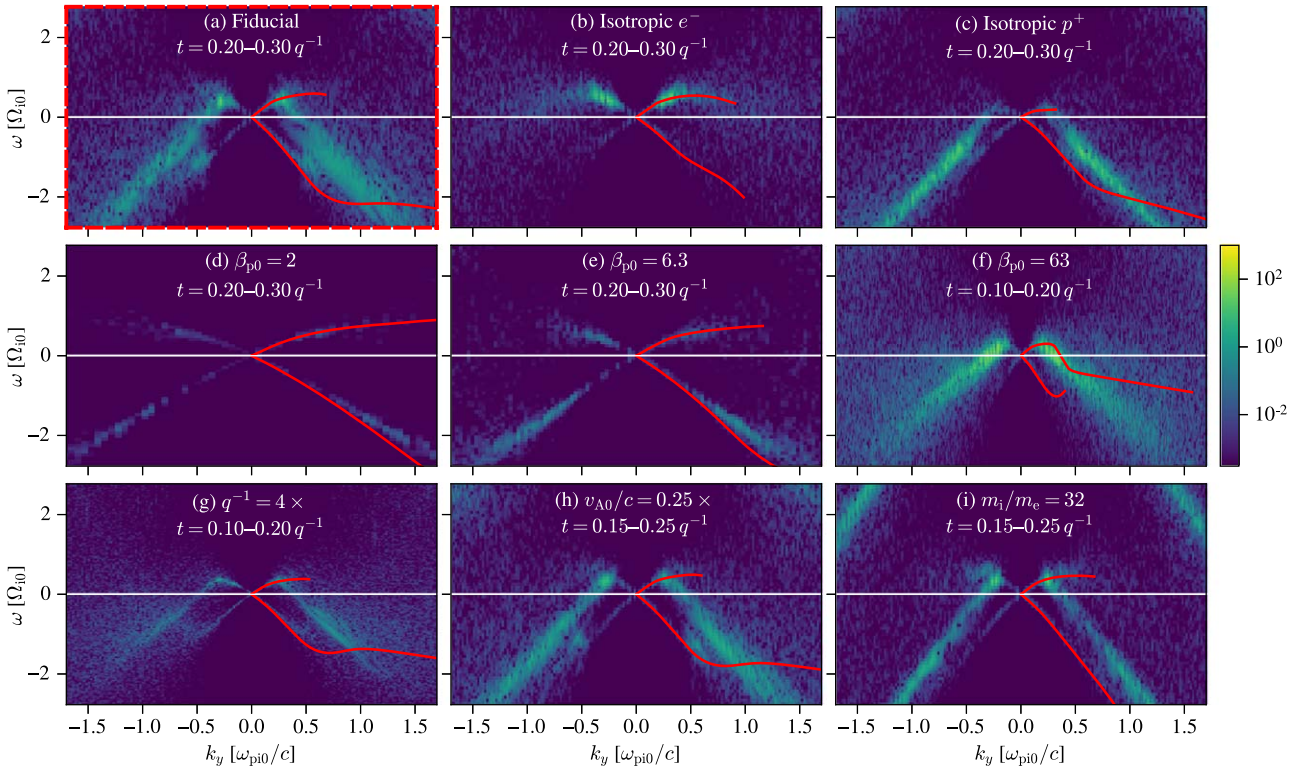

Figure 15. The RCP wave offset is a high-$\beta_{\rm p}$ effect driven by anisotropic electrons in the presence of hot ions, which we show by plotting (ω, k) power spectra, at early times in the simulation when RCP waves are first excited, for eight simulations altered in one or a few parameters with respect to our fiducial simulation. Like Figure 2, RCP/LCP wave power has $\omega > 0$ and < 0, respectively; the red curves are the whistler and IC dispersion curves, truncated at strong damping $\Gamma(k) < -|\omega(k)|$. (a) Fiducial simulation, same as Figure 2(a). (b) Isotropic electrons using $q_{\rm iso} = 2q/3$. (c) Isotropic protons using $q_{\rm iso} = 2q/3$. (d)–(f) Initial total plasma beta $\beta_{\rm p0} = 2$, 6.3, and 63. (g) Slower compression with $q^{-1} = 4\times$ larger than the fiducial simulation. (h) Lower $v_{\rm A0}/c$ by a factor $0.25\times$ with respect to the fiducial simulation; i.e., less relativistic. (i) Raise $m_{\rm i}/m_{\rm e} = 32$ and lower $v_{\rm A0}/c$, same simulation as that shown in Figure 14(h). Panels (f)–(i) have different time selections because altering $\beta_{\rm p0}$, q^{-1}, $v_{\rm A0}/c$, and $m_{\rm i}/m_{\rm e}$ also alters the time of appearance of the RCP offset waves.

Appendix C
Why do Waves Form Two Frequency Bands?

We perform four numerical experiments to check the origin of the two distinct frequency bands of wave power in Figure 1(a).

First, we halt the compression at $t = 0.5q^{-1}$ and $t = 1.0q^{-1}$. The scale factors $a_x(t)$ and $a_z(t)$ (Equation (3)) are pinned to constants; the waves and particles are allowed to evolve self-consistently without further external driving.

The result is shown by Figures 16(a), (c), (i) and (c), (g), (k). The existing wave power drifts toward lower frequencies, while the high-frequency band either does not appear as a distinct feature (Figure 16(a)) or weakens in strength (Figure 16(c)) as compared to Figure 1(a).

Then, we halt compression and also "reset" waves to see (i) what waves are driven unstable by the particles' own anisotropic distribution, and (ii) if said waves are reasonably predicted by the nonrelativistic bi-Maxwellian approximation of Equation (8). To "reset" waves, we zero all electromagnetic fields except for the background field B_g. We also subtract all particles' bulk motion as follows. We compute the ion and electron bulk three-velocities with a five-cell kernel for particle-to-grid mapping. All macroparticles are Lorentz boosted so as to cancel their own species' bulk velocity; their PIC weights are also adjusted to account for the spatial part of the Lorentz transformation (Zenitani 2015). The velocity subtraction is not perfect; it leaves a residual bulk motion at a few percent of its original amplitude. Therefore, we apply the same velocity subtraction procedure again. Two velocity subtractions suffice to leave no detectable ion bulk motion.

The result of halting compression and resetting waves is shown by Figures 16(b), (f), (j) and (d), (h), (l). The anisotropic particle distributions grow waves in a comparatively "high" frequency band consistent with the unstable wave prediction of Equation (8).

Appendix D
Scattering Measurement Time Step

To measure pitch-angle scattering in Figure 3, the measurement time step Δt cannot be too short or too long.

If Δt is too short, an electron may not have time to interact with one or multiple waves; its trajectory in momentum space may not yet be diffusive. The relativistic cyclotron frequency is $eB/(\gamma\ m_e\ c) \sim \Omega_i$ for $p/(m_e\ c) \sim 10$ and $m_i/m_e = 8$, so a time step $\Delta t \gtrsim$ a few Ω_{i0}^{-1} should suffice to resolve the wave–particle interaction. More energetic electrons with larger γ and hence slower gyration may need a correspondingly longer time step.

If Δt is too long, electrons may scatter out of the wave resonance and experience very different scattering rates within the measurement time Δt; our measurement becomes nonlocal in μ. The wave resonance region itself may evolve in time. Additionally, electron displacements in μ may become comparable to the finite range of $\mu \in [-1, 1]$; our measurement of $\langle \Delta\mu\Delta\mu \rangle$ would trend toward a constant rather than increasing linearly with Δt as expected for an unbounded random walk.

In Figure 17, we show how altering Δt by $0.2\times$ to $10\times$ (i.e., $0.9\Omega_{i0}^{-1}$ to $47\Omega_{i0}^{-1}$) alters the measured scattering rates $\langle \Delta\mu\Delta\mu \rangle / (2\Delta t)$ in phase-space coordinates $(p, |\mu|)$. Recall our fiducial $\Delta t = 4.7\Omega_{i0}^{-1}$ in Figure 3.

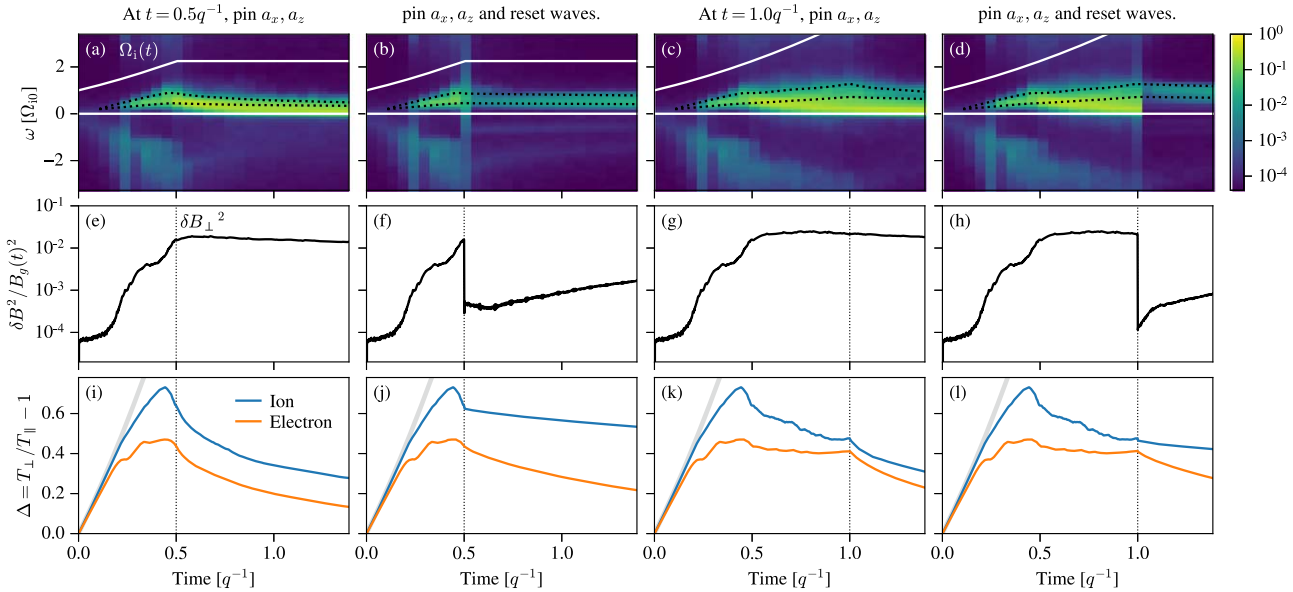

Figure 16. Halt compression and/or reset waves in the fiducial simulation (procedure given in Appendix C), to test the origin of low- and high-frequency LCP wave power in Figure 1(a). The panel layout matches Figures 1(a), (c), and (d): the top row is the wave spectrogram, the middle row is the magnetic fluctuation power scaled to the background field $B_g(t)$, and the bottom row is the ion and electron anisotropy Δ. In the left two columns, compression halts at $t = 0.5q^{-1}$; in the right two columns, compression halts at $t = 1.0q^{-1}$. In panels (a) and (c), when compression halts, low-frequency wave power persists and high-frequency power weakens or does not appear. In panels (b) and (d), when compression halts and waves are also reset, the particle thermal anisotropy drives waves in the unstable frequency band predicted by Equation (8) (black dotted lines), and lower-frequency wave power does not appear.

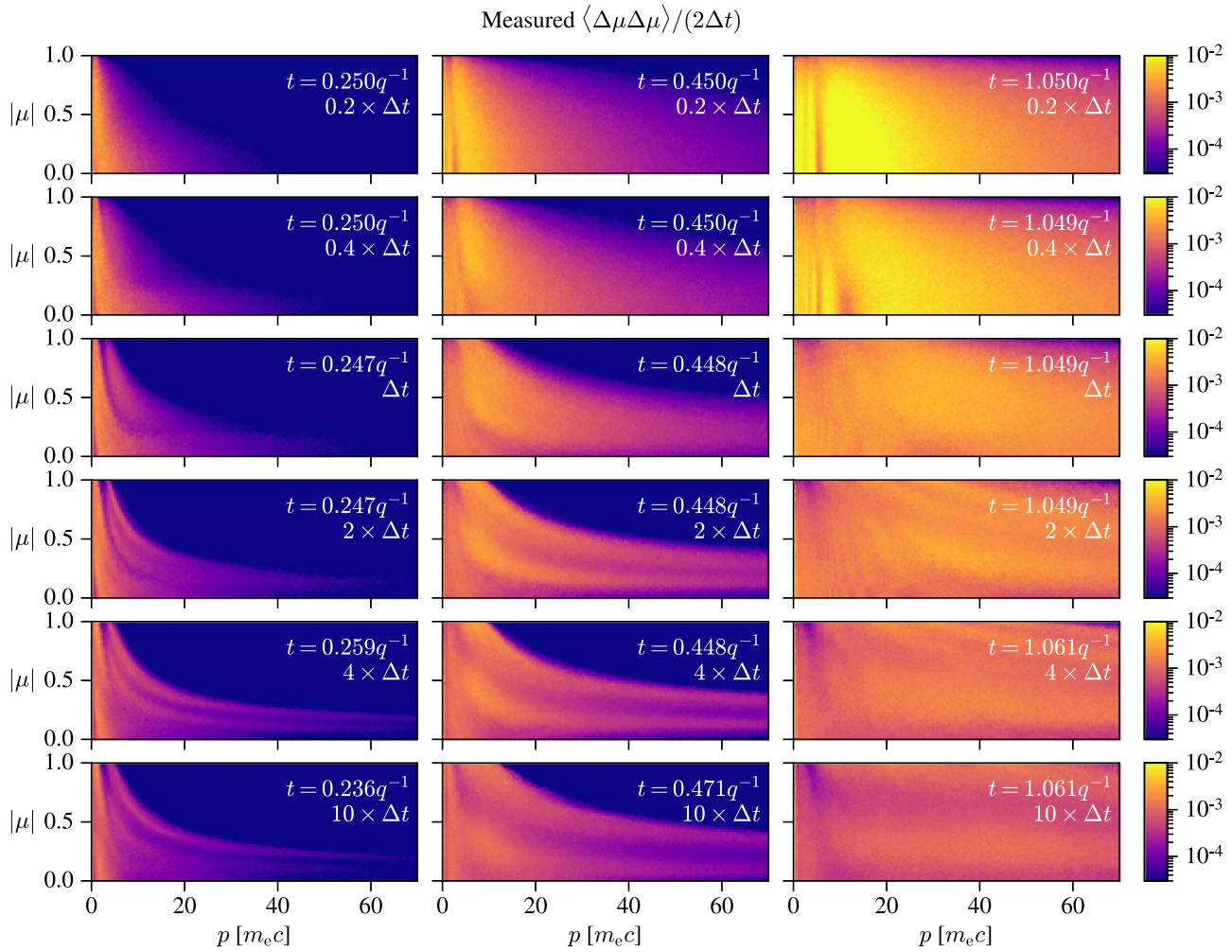

Figure 17. Effect of varying Δt upon the measured pitch-angle scattering rate, measured between times t and $t + \Delta t$. The scattering time step Δt is smallest at the top and increases going down each row, varying from 0.9 to $47\Omega_{i0}^{-1}$; the third row from the top corresponds to $\Delta t = 4.7\Omega_{i0}^{-1}$ as used for Figures 3(j), (k), (l). The simulation time varies from left to right columns as $t \approx 0.25q^{-1}$, $0.45q^{-1}$, and $1.05q^{-1}$ to match Figure 3.

Appendix E
Numerical Convergence

In Figure 18 we show numerical convergence with respect to the number of particles per cell, focusing on the total wave power $\delta B_\perp{}^2$, ion temperature anisotropy Δ_i, and electron temperature anisotropy Δ_e. In particular, we sample these quantities at $t = 1q^{-1}$ in order to check convergence at late times when waves scatter CRe appreciably. We check convergence for our fiducial simulation and also all runs with varying q^{-1}, v_{A0}/c, and m_i/m_e. The simulations in Figure 18 used single-precision floats for particle momenta in the PIC algorithm, which introduces a small numerical error (see Section 2). This precision error does not depend on particle sampling, so we consider it acceptable for our convergence test.

It is most important that the wave power and ion temperature anisotropy are converged with respect to the particle sampling for our study. For all simulations considered, a 2 or 4 times increase in the particle count does not modify $\delta B_\perp{}^2$ or Δ_i by more than a factor of 1.5×. We consider this rate of convergence acceptable.

The electron temperature anisotropy is more sensitive to particle sampling. Some simulations are not converged in Δ_e, in particular those with large q^{-1}. We consider this incomplete convergence acceptable because of the minor role of electron-driven waves in CRe energization, as shown by our simulations of CRe energy gain with electrons heated isotropically to prevent whistler wave growth (Figures 14(i)–(l)).

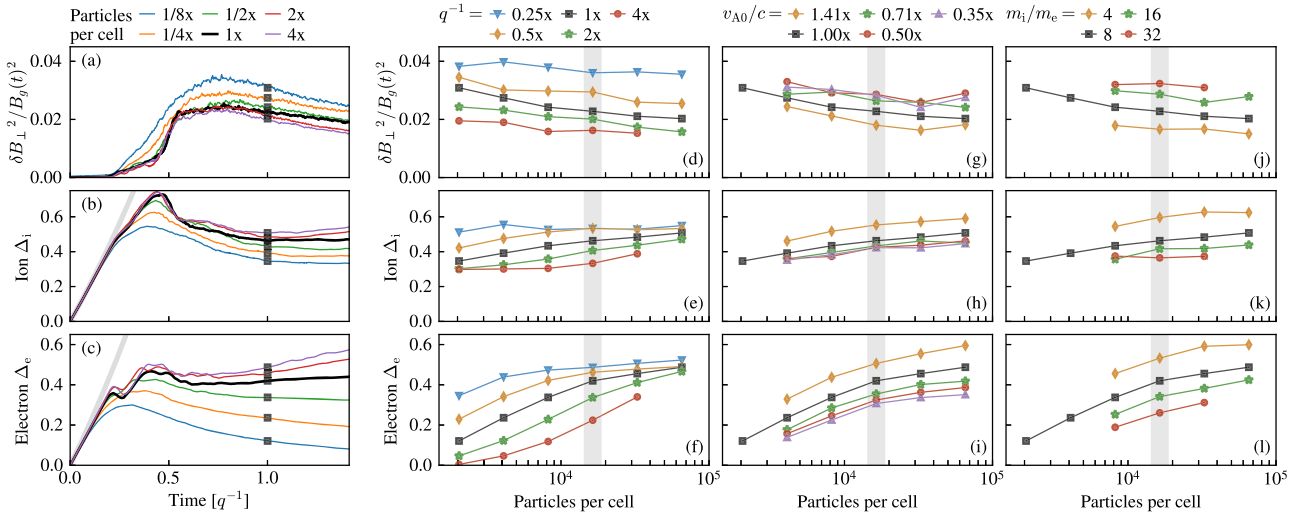

Figure 18. Convergence of our simulations with respect to particle sampling for thermal ICM particles (both ions and electrons). Left-most column: time-evolving (a) wave power $\delta B_\perp{}^2$, (b) ion anisotropy Δ_i, and (c) electron anisotropy Δ_e for varying particles per cell (colored curves) compared to our fiducial simulation (black curve). Thick light-gray curve is nonrelativistic CGL prediction in (b)–(c). The black squares at $t = 1q^{-1}$ correspond to the same symbols in (d)–(l). Right three columns: wave power and anisotropy, measured at $t = 1q^{-1}$ for simulations with varying q^{-1} (d)–(f), v_{A0}/c (g)–(i), and m_i/m_e (j)–(l). Each marker set represents one simulation from the main article with varied particle sampling. The black squares represent fiducial simulation in all panels (d)–(l), and correspond to the data and markers in (a)–(c). The vertical light-gray bar indicates the fiducial particle sampling of 16,384 ions and electrons per cell (excluding test-particle CRe); all markers within the light-gray bar correspond to a simulation from the main article (see Table 1). The legends above each column report the ratio of q^{-1}, v_{A0}/c, and m_i/m_e with respect to the fiducial simulation (1×).

Appendix F
Simulation Parameters

Table 1 provides the input parameters for all simulations in this article: first the fiducial simulation, followed by parameter sweeps of q^{-1}, $k_B\,T_0$ (equivalently v_{A0}/c), m_i/m_e, and β_{p0}. The simulations with varying β_{p0} are only used in Appendix B. Simulations with varying particle count (Appendix E) or with one species isotropic are not explicitly shown.

We define some input parameters in code units: `my` is the domain size in cells; `intv` is the number of time steps between output file dumps, relevant for wave-power spectra and particle scattering measurements; `dur` is the simulation duration in time steps. Other key parameters such as the grid cell size, particles per cell, current filtering, and numerical speed of light are identical across all simulations and are stated in Section 2.

Table 1
Simulation Input Parameters

Purpose	m_i/m_e	β_{p0}	$k_B\,T_0$ $[m_e c^2]$	v_{A0}/c	q^{-1} $[\Omega_{i0}^{-1}]$	my	my $[\rho_{i0}]$	intv	intv $[\Omega_{i0}^{-1}]$	dur	dur $[q^{-1}]$
Fiducial	8	20.0	0.20	0.067	800	4608	79.3	800	0.94	960000	1.41
Vary q^{-1}	8	20.0	0.20	0.067	200	4608	79.3	800	0.94	240000	1.41
Vary q^{-1}	8	20.0	0.20	0.067	400	4608	79.3	800	0.94	480000	1.41
Vary q^{-1}	8	20.0	0.20	0.067	1600	4608	79.3	800	0.94	1920000	1.41
Vary q^{-1}	8	20.0	0.20	0.067	3200	4608	79.3	800	0.94	3840000	1.41
Vary v_{A0}/c	8	20.0	0.40	0.094	800	4608	79.3	600	1.00	720000	1.50
Vary v_{A0}/c	8	20.0	0.10	0.047	800	4608	79.3	1200	1.00	1440000	1.50
Vary v_{A0}/c	8	20.0	0.05	0.033	800	4608	79.3	1700	1.00	2040000	1.50
Vary v_{A0}/c	8	20.0	0.03	0.024	800	4608	79.3	2400	1.00	2880000	1.50
Vary m_i/m_e	4	20.0	0.20	0.089	800	3840	88.7	400	0.89	480000	1.34
Vary m_i/m_e	16	20.0	0.20	0.049	800	6144	77.0	1600	0.97	1920000	1.46
Vary m_i/m_e	32	20.0	0.20	0.035	800	9216	82.8	3200	0.98	3840000	1.48
Vary β_{p0}	8	2.0	0.20	0.211	800	1536	83.6	300	1.12	360000	1.68
Vary β_{p0}	8	6.3	0.20	0.119	800	2688	82.3	500	1.05	600000	1.57
Vary β_{p0}	8	63.2	0.20	0.037	800	8192	79.3	1500	0.99	1800000	1.49

Note. The columns are defined in Section 2 and Appendix F.

(This table is available in machine-readable form.)

ORCID iDs

Aaron Tran https://orcid.org/0000-0003-3483-4890
Lorenzo Sironi https://orcid.org/0000-0002-1227-2754
Francisco Ley https://orcid.org/0000-0002-8820-8177
Ellen G. Zweibel https://orcid.org/0000-0003-4821-713X
Mario A. Riquelme https://orcid.org/0000-0003-2928-6412

References

Abramopoulos, F., Chanan, G. A., & Ku, W. H. M. 1981, ApJ, 248, 429
Adair, L., Angelopoulos, V., Sibeck, D., & Zhang, X. J. 2022, JGRA, 127, e29790
Albert, J. M., & Bortnik, J. 2009, GeoRL, 36, L12110
Alfvén, H. 1950, PhRv, 77, 375
Arzamasskiy, L., Kunz, M. W., Squire, J., Quataert, E., & Schekochihin, A. A. 2023, PhRvX, 13, 021014
Bale, S. D., Kasper, J. C., Howes, G. G., et al. 2009, PhRvL, 103, 211101
Berger, J. M., Newcomb, W. A., Dawson, J. M., et al. 1958, PhFl, 1, 301
Berlok, T., & Pessah, M. E. 2015, ApJ, 813, 22
Birdsall, C. K., & Langdon, A. B. 1991, Plasma Physics via Computer Simulation (Bristol: Institute of Physics Publishing)
Blasi, P. 2000, ApJL, 532, L9
Borovsky, J. E. 1986, PhFl, 29, 3245
Borovsky, J. E., Goertz, C. K., & Joyce, G. 1981, JGR, 86, 3481
Borovsky, J. E., Horne, R. B., & Meredith, N. P. 2017, JGRA, 122, 12072
Böss, L. M., Steinwandel, U. P., Dolag, K., & Lesch, H. 2023, MNRAS, 519, 548
Bott, A. F. A., Arzamasskiy, L., Kunz, M. W., Quataert, E., & Squire, J. 2021, ApJL, 922, L35
Brunetti, G., Blasi, P., Cassano, R., & Gabici, S. 2004, MNRAS, 350, 1174
Brunetti, G., & Lazarian, A. 2007, MNRAS, 378, 245
Brunetti, G., & Lazarian, A. 2011, MNRAS, 412, 817
Brunetti, G., & Lazarian, A. 2016, MNRAS, 458, 2584
Brunetti, G., Setti, G., Feretti, L., & Giovannini, G. 2001, MNRAS, 320, 365
Brunetti, G., & Vazza, F. 2020, PhRvL, 124, 051101
Buneman, O. 1993, in Computer Space Plasma Physics: Simulation Techniques and Software, ed. H. Matsumoto & Y. Omura (Tokyo: Terra Scientific), 67
Chen, C. H. K., Matteini, L., Schekochihin, A. A., et al. 2016, ApJL, 825, L26
Chen, Y., Reiprich, T. H., Böhringer, H., Ikebe, Y., & Zhang, Y. Y. 2007, A&A, 466, 805
Chew, G. F., Goldberger, M. L., & Low, F. E. 1956, RSPSA, 236, 112
Davidson, R. C., & Ogden, J. M. 1975, PhFl, 18, 1045
dos Santos, M. S., Ziebell, L. F., & Gaelzer, R. 2015, PhPl, 22, 122107
Egedal, J., & Lichko, E. 2021, JPlPh, 87, 905870610
Egedal, J., Schroeder, J., & Lichko, E. 2021, JPlPh, 87, 905870116
Enßlin, T. A. 1999, Diffuse Thermal and Relativistic Plasma in Galaxy Clusters, ed. H. Boehringer, L. Feretti, & P. Schuecker, (Garching: Max-Planck-Institut fur Extraterrestrische Physik), 275
Enßlin, T. A., & Gopal-Krishna 2001, A&A , 366, 26
Felice, G. M., & Kulsrud, R. M. 2001, ApJ, 553, 198
Fermi, E. 1949, PhRv, 75, 1169
Fowler, C. M., Agapitov, O. V., Xu, S., et al. 2020, GeoRL, 47, e86408
Fox, D. C., & Loeb, A. 1997, ApJ, 491, 459
Fried, B. D., & Conte, S. D. 1961, The Plasma Dispersion Function (New York: Academic)
Gary, S. P., Convery, P. D., Denton, R. E., Fuselier, S. A., & Anderson, B. J. 1994a, JGR, 99, 5915
Gary, S. P., Fuselier, S. A., & Anderson, B. J. 1993, JGR, 98, 1481
Gary, S. P., & Karimabadi, H. 2006, JGRA, 111, A11224
Gary, S. P., & Lee, M. A. 1994, JGR, 99, 11297
Gary, S. P., McKean, M. E., Winske, D., et al. 1994b, JGR, 99, 5903
Gary, S. P., & Wang, J. 1996, JGR, 101, 10749
Gaspari, M., & Churazov, E. 2013, A&A, 559, A78
Goertz, C. K. 1978, JGR, 83, 3145
Guo, X., Sironi, L., & Narayan, R. 2014, ApJ, 794, 153
Ha, J.-H., Ryu, D., Kang, H., & Kim, S. 2022, ApJ, 925, 88
Hellinger, P. 2007, PhPl, 14, 082105
Hellinger, P., & Trávníček, P. 2005, JGRA, 110, A04210
Hellinger, P., Trávníček, P., Kasper, J. C., & Lazarus, A. J. 2006, GeoRL, 33, L09101
Hellinger, P., Trávníček, P., Mangeney, A., & Grappin, R. 2003, GeoRL, 30, 1211
Holcomb, C., & Spitkovsky, A. 2019, ApJ, 882, 3
Innocenti, M. E., Tenerani, A., & Velli, M. 2019, ApJ, 870, 66
Isenberg, P. A., Maruca, B. A., & Kasper, J. C. 2013, ApJ, 773, 164
Jokipii, J. R. 1966, ApJ, 146, 480
Kang, H., & Ryu, D. 2016, ApJ, 823, 13
Kang, H., Ryu, D., & Jones, T. W. 2012, ApJ, 756, 97
Kasper, J. C., Lazarus, A. J., & Gary, S. P. 2002, GeoRL, 29, 1839
Kennel, C. F., & Engelmann, F. 1966, PhFl, 9, 2377
Kennel, C. F., & Petschek, H. E. 1966, JGR, 71, 1
Kulsrud, R., & Pearce, W. P. 1969, ApJ, 156, 445
Kunz, M. W., Schekochihin, A. A., & Stone, J. M. 2014, PhRvL, 112, 205003
Kunz, M. W., Squire, J., Balbus, S. A., et al. 2019, arXiv:1903.04080
Kunz, M. W., Squire, J., Schekochihin, A. A., & Quataert, E. 2020, JPlPh, 86, 905860603
Ley, F., Riquelme, M., Sironi, L., Verscharen, D., & Sandoval, A. 2019, ApJ, 880, 100
Ley, F., Zweibel, E. G., Riquelme, M., et al. 2023, ApJ, 947, 89
Lichko, E., & Egedal, J. 2020, NatCo, 11, 2942
Lichko, E., Egedal, J., Daughton, W., & Kasper, J. 2017, ApJL, 850, L28
Liewer, P. C., Velli, M., & Goldstein, B. E. 2001, JGR, 106, 29261
Liu, K., Lemons, D. S., Winske, D., & Gary, S. P. 2010, JGRA, 115, A04204
Markevitch, M., Govoni, F., Brunetti, G., & Jerius, D. 2005, ApJ, 627, 733
Markovskii, S. A., Vasquez, B. J., & Chandran, B. D. G. 2020, ApJ, 889, 7
Matsukiyo, S., & Hada, T. 2009, ApJ, 692, 1004
Melville, S., Schekochihin, A. A., & Kunz, M. W. 2016, MNRAS, 459, 2701
Meredith, N. P., Thorne, R. M., Horne, R. B., et al. 2003, JGRA, 108, 1250
Mernier, F., Biffi, V., Yamaguchi, H., et al. 2018, SSRv, 214, 129
Northrop, T. G. 1963, RvGSP, 1, 283
Peng, F., & Nagai, D. 2009, ApJ, 693, 839
Petrosian, V. 2001, ApJ, 557, 560
Pinzke, A., Oh, S. P., & Pfrommer, C. 2013, MNRAS, 435, 1061
Riquelme, M., Quataert, E., & Verscharen, D. 2018, ApJ, 854, 132
Schlüter, A. 1957, ZNatA, 12, 822
Schwartz, S. J., Burgess, D., & Moses, J. J. 1996, AnGeo, 14, 1134
Shoji, M., Omura, Y., Tsurutani, B. T., Verkhoglyadova, O. P., & Lembege, B. 2009, JGRA, 114, A10203
Sironi, L., & Narayan, R. 2015, ApJ, 800, 88
Smith, R. L., & Brice, N. 1964, JGR, 69, 5029
Spitkovsky, A. 2005, in AIP Conf. Proc. 801, Astrophysical Sources of High Energy Particles and Radiation, ed. T. Bulik, B. Rudak, & G. Madejski (Melville, NY: AIP), 345
Stix, T. H. 1992, Waves in Plasmas (Melville, NY: AIP)
Summers, D. 2005, JGRA, 110, A08213
Terasawa, T., & Matsukiyo, S. 2012, SSRv, 173, 623
Thorne, R. M., & Kennel, C. F. 1971, JGR, 76, 4446
Tonoian, D. S., Artemyev, A. V., Zhang, X.-J., Shevelev, M. M., & Vainchtein, D. L. 2022, PhPl, 29, 082903
Tsurutani, B. T., & Lakhina, G. S. 1997, RvGeo, 35, 491
van Weeren, R. J., Andrade-Santos, F., Dawson, W. A., et al. 2017, NatAs, 1, 0005
van Weeren, R. J., de Gasperin, F., Akamatsu, H., et al. 2019, SSRv, 215, 16
Yoon, P. H., Seough, J. J., Khim, K. K., et al. 2010, PhPl, 17, 082111
Zenitani, S. 2015, PhPl, 22, 042116
Zhang, X. J., Li, W., Ma, Q., et al. 2016, JGRA, 121, 6620
Zweibel, E. G. 2020, ApJ, 890, 67